Department of Physics and Astronomy
Heidelberg University

Bachelor Thesis in Physics
submitted by

Sophie Rohletter

born in Weilburg (Germany)

2021

First look at J/ψ production in TRD - triggered pp collisions at $\sqrt{s}$ = 13 TeV with ALICE

This Bachelor Thesis has been carried out by Sophie Rohletter at the
Physikalisches Institut in Heidelberg
under the supervision of
Priv. Doz. Dr. Yvonne Pachmayer.

Abstract

This thesis examines the yield of the J/ψ meson in the di-electron channel measured in proton-proton collisions at a center-of-mass energy of $\sqrt{s} = 13$ TeV. The analyzed sample includes events triggered by the Transition Radiation Detector in ALICE taken in 2017 and 2018 and contains about 126 million events. The particle identification is done by the Time Projection Chamber in the central barrel of ALICE. For that, the standard deviation of the measured energy loss from the theoretical prediction by Bethe-Bloch is post calibrated to select electron tracks. A runwise quality assurance for events and tracks is done to examine whether the behaviour of the data is reasonable and described well by Monte Carlo simulations. Finally, the raw J/ψ signal is obtained by subtracting the uncorrelated and the correlated background from the invariant mass distribution of electron-positron pairs and counting bins in the window $2.921 < m_{\mathrm{inv.},e^+e^-} < 3.159$ GeV/c^2. For $p_T > 2$ GeV/c an uncorrected p_T integrated J/ψ yield is obtained, as well as an uncorrected p_T differential yield.

Zusammenfassung

Im Rahmen dieser Bachelorarbeit wird das Signal des J/ψ Mesons im di-elektronischen Zerfallskanal untersucht. Dazu wird in Proton-Proton Kollisionen bei einer Schwerpunktsenergie von $\sqrt{s} = 13$ TeV gemessen. Die analysierten Daten beinhalten Events, die vom Übergangsstrahlungsdetektor in ALICE 2017 und 2018 gemessen wurden und umfassen etwa 126 Millionen Events. Die Teilchenidentifikation wird mit Hilfe der Zeitprojektionskammer gemacht. Die Standardabweichung des gemessenen Energieverlusts von der theoretischen Vorhersage durch Bethe-Bloch wird nachkalibriert, um Spuren, die Elektronen enthalten, zu identifizieren. Es wird eine Qualitätssicherung von Events und Spuren für jeden Run durchgeführt, um zu überprüfen, ob die Daten sinnvoll sind und gut durch Monte Carlo Simulationen beschrieben werden. Schließlich erhält man das J/ψ Signal durch Subtraktion des unkorrelierten und des korrelierten Hintergrunds vom invarianten Massenspektrum von Elektron-Positron Paaren und durch Zählen der Einträge im Bereich $2.921 < m_{\mathrm{inv.},e^+e^-} < 3.159$ GeV/c^2. Für $p_T > 2$ GeV/c erhalten wir ein unkorrigiertes p_T integriertes Signal und ein unkorrigiertes p_T differenziertes Signal.

Contents

List of Acronyms

ALICE	A Large Ion Collider Experiment
BNL	Brookhaven National Laboratory
CERN	European Organization for Nuclear Research
DCA	Distance of Closest Approach
GTU	Global Tracking Unit
ITS	Inner Tracking System
LHC	Large Hadron Collider
LS	Like-Sign
MC	Monte Carlo
ME	Mixed Event
MIP	Minimum Ionizing Particle
MWPC	Muli Wire Proportional Chamber
PID	Particle Identification
SM	Standard Model
SDD	Silicon Drift Detector
SE	Same Event
SLAC	Stanford Linear Accelerator Center
SPD	Silicon Pixel Detector
SSD	Silicon Strip Detector
US	Unlike-Sign
TPC	Time Projection Chamber
TRD	Transition Radiation Detector
QA	Quality Assurance
QCD	Quantum Chromodynamics
QGP	Quark-Gluon Plasma

Chapter 1

Introduction and Theoretical Background

1.1 Motivation

In the collisions of hadrons, as collision energy increases, the production cross section of $c\bar{c}$ gets larger which leads to a higher production rate of hadrons that contain c quarks. The statistical hadronisation model predicts that the R_{AA} of J/ψ, which is defined as the relative production in Pb-Pb collisions compared to pp collisions, is larger at high energies than what was observed at lower collision energies as explained in [11]. Recent J/ψ R_{AA} measurements from the ALICE collaboration presented in [9] are well agreed with this prediction which implies that there is a substantial contribution of J/ψ mesons produced by regeneration. Improved precision measurements of the R_{AA} will allow us to study this observation in more detail. For that, it is crucial to have a precise measurement in pp collisions as a reference. In addition, the production mechanism of J/ψ in pp collisions is still unclear and needs experimental measurements for the validation of theoretical predictions.

1.2 The Standard Model

In order to understand the processes of particle production, particle decay and the interaction of particles with matter, i.e. the detector material, we first need to introduce the basic principles of the Standard Model (SM) of particle physics as described in [20].

The SM is schematically shown in Figure 1.1 and consists of 17 particles. It can be subdivided into two categories of particles called fermions and bosons. The twelve fermions and their anti-particles, that have the same mass and opposite charge, have spin 1/2. They are complemented by four gauge bosons, which carry the fundamental forces and have spin 1, and by the Higgs boson with spin 0.

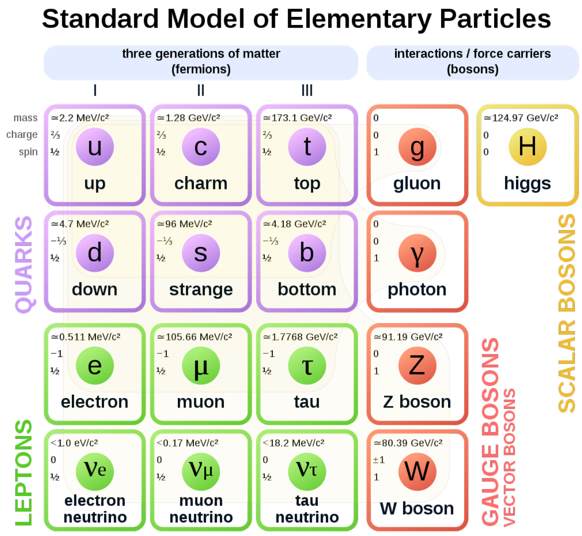

Figure 1.1: The Standard Model of particle physics with its twelve fermions and five bosons. Figure taken from [2].

The fermions can be categorized into two groups of six particles each, namely quarks and leptons. They are sorted in three rows, which are the so-called generations, that correspond to same properties like charge and spin, only differing in mass. The higher the generation of a particle, the higher is its mass. An important difference between the two categories is the free existence of leptons, while quarks are confined to color neutral bound states called hadrons. Confinement results from the nature of the strong force and is described in quantum chromodynamics (QCD). Even though, the existence of quarks was measured in several experiments, free quarks were never detected. Only bound states are observed, which can be subdivided into two groups: mesons which consist of a quark and an anti-quark (e.g. $\pi^{\pm}$, π^0, $K^{\pm}$, K^0, J/ψ) and baryons that are made of three quarks or three antiquarks (e.g. p, n, Λ^0, Δ^0).

The interaction between fermions can be described by the four fundamental forces: strong, electromagnetic and weak interaction as well as gravity. Gravity is not included in the SM, but the other three are represented by gauge bosons as mediators: the strong interaction by the gluon, the electromagnetic interaction by the photon and the weak interaction by the charged $W^{\pm}$ bosons and the neutral Z boson.

1.3 Quantum Chromodynamics

The exchange particle of the strong interaction is the gluon, that carries the so-called color charge. It is only experienced by particles that carry color charge themselves, i.e. quarks and other gluons. There are three different types of color charge states: red, blue and green and the corresponding anti-colors. Since the strong interaction describes the coupling of a gluon to other particles that carry color charge and it is a color charge carrier itself, gluon self-interaction is possible. This results in a constant energy density between the two initial particles. Hence, the energy stored in the color field between them is proportional to their distance to each other. This explains the high amount of energy for the separation of quarks and leads to confinement and the formation of hadrons. Another property of QCD is the asymptotic freedom which indicates that the coupling constant of the strong interaction decreases for larger energy transfer or decreasing length scale until the particles behave as asymptotically free particles. This effect is known as running of the coupling constant and is confirmed experimentally as shown in Figure 1.2. This allows that quarks can exist in quasi-free states if temperature and pressure are high enough. In ultra-relativistic heavy-ion collisions, such extreme conditions of high energy densities and temperatures can be achieved for a short amount of time and create unconfined matter, called the quark-gluon plasma (QGP). We can observe its physical properties and the transition back to confined matter known as hadronisation.

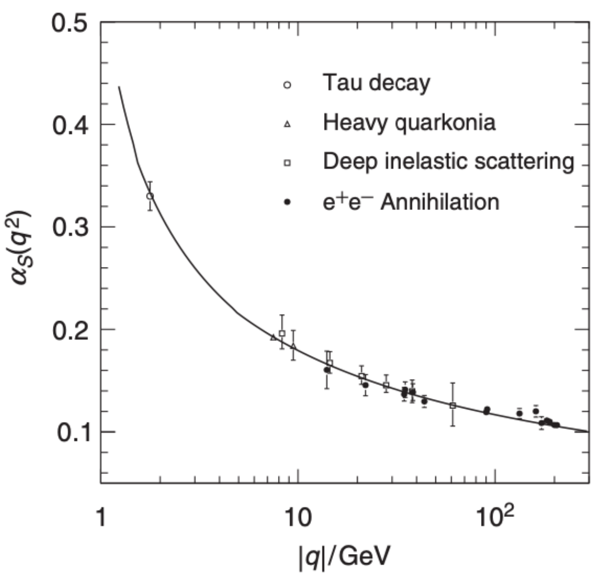

Figure 1.2: Measurements of the strong coupling α_s at different $|q|$ scales. Figure taken from [20].

1.4 The J/ψ Meson

The existence of a fourth quark flavor, namely the charm flavor, was early hypothesized on a theoretical basis, i.e. the GIM mechanism as explained in [14]. The first experimental observation was not until 1974, when the J/ψ, a charmonium state, i.e. the bound state of a charm quark and a charm antiquark, was discovered. There were two groups that announced the discovery simultaneously: one at Brookhaven National Laboratory (BNL) [4] and the other one at the Stanford Linear Accelerator Center (SLAC) [5]. At BNL, a proton beam was shot against a beryllium target and a sharp peak in the invariant mass spectrum of e^+e^- was observed. At SLAC, a resonance in the annihilation of e^+e^- was observed in hadronic and leptonic channels. The J/ψ has a width of $\Gamma = (92.6 \pm 1.7)$ keV$/c^2$ and a mass of $m = (3096.900 \pm 0.006)$ MeV$/c^2$ as published in [23].

The discovery of the J/ψ started a revolution in the world of particle physics and it still is a particle of interest today as its production mechanism is not completely understood. The precise measurement of J/ψ production can be the input for the theoretical development. Furthermore, this measurement will provide a reference for the production in p-Pb and Pb-Pb collisions, which can be modified by the presence of the QGP as explained in [17, 11].

As the J/ψ is not a stable particle, it decays shortly after the production. The branching ratios of the different decay channels can be seen in Figure 1.3.

$J/\psi(1S)$ DECAY MODES

	Mode		Fraction (Γ_i/Γ)	Scale factor/ Confidence level
Γ_1	hadrons		(87.7 ± 0.5) %	
Γ_2	virtual $\gamma \to$ hadrons		(13.50 ± 0.30) %	
Γ_3	ggg		(64.1 ± 1.0) %	
Γ_4	γgg		(8.8 ± 1.1) %	
Γ_5	e^+e^-		(5.971 ± 0.032) %	
Γ_6	$e^+e^-\gamma$	[a]	$(8.8 \pm 1.4) \times 10^{-3}$	
Γ_7	$\mu^+\mu^-$		(5.961 ± 0.033) %	

Figure 1.3: Decay channels and Branching Ratios of the most important J/ψ decay modes. Table taken from [23].

We will later use the decay channel into e^+e^- for analyzing the data, as it has less background than the hadronic channel and can be triggered by the TRD.

1.5 Particle Detection

To detect particles and measure their properties, we need to measure their interaction with the detector material. When a charged particle traverses the detector material, it is subject to random collisions with the atoms/molecules. The mean distance between two such interactions is characterized by the mean free path

$$\lambda = \frac{1}{n_e \sigma}, \tag{1.1}$$

where n_e is the electron density of the medium and σ is the total collision cross section. Since this process is random, the number of collisions n can be quantified by a Poisson distribution

$$P(x/\lambda, n) = \frac{(x/\lambda)^n}{n!} \cdot e^{-x/\lambda}. \tag{1.2}$$

These collisions may cause an ionization of the atom or molecule. If the energy transfer is sufficient this results in the liberation of a primary electron. The mean energy loss via ionization per unit path length is quantified by the Bethe-Bloch formula as defined in [16]:

$$\left\langle -\frac{dE}{dx} \right\rangle = Kz^2 \frac{Z}{A} \frac{1}{\beta^2} \left[\frac{1}{2} \ln\left(\frac{2m_e c^2 \beta^2 \gamma^2 W_{max}}{I^2} \right) - \beta^2 - \frac{\delta(\beta\gamma)}{2} \right] \tag{1.3}$$

z:	charge of incident particle
K:	constant factor
Z:	charge number of traversed medium
A:	atomic mass of traversed medium
m_e:	electron mass
c:	speed of light
I:	mean excitation energy of traversed medium
δ:	density correction of traversed medium
W_{max}:	maximum energy transfer in a single collision

Here, $\beta = v/c$ stands for the relative velocity and $\gamma = \frac{1}{\sqrt{1-\beta^2}}$ for the Lorentz factor of the incident particle. Since the mean energy loss described by Bethe-Bloch depends on β and γ and hence on the velocity, particles with different masses and equal β and γ correspond to different momenta $p = \beta\gamma m$ and thus different energy loss $\mathrm{d}E/\mathrm{d}x$ as shown in Figure 1.4. This can be used as a reference for the experimental measurements and allows to assign a track to a corresponding particle band.

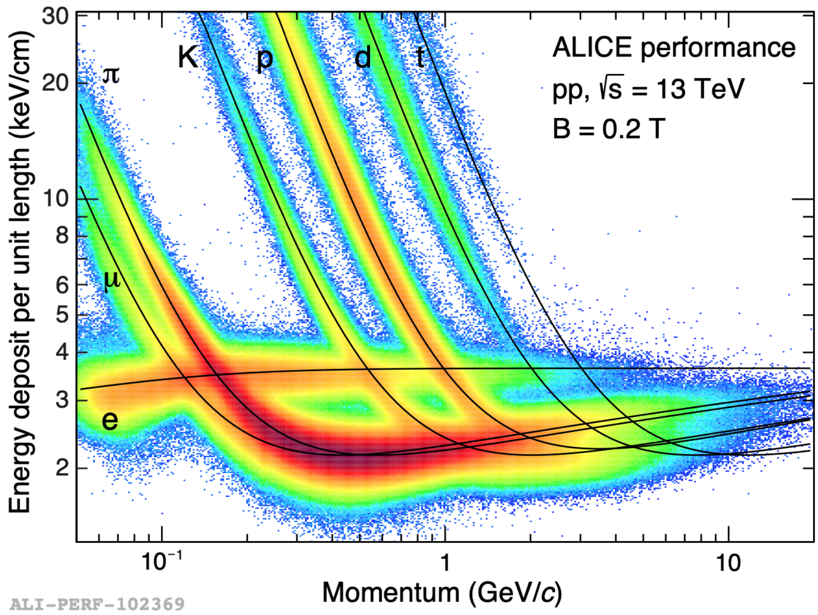

Figure 1.4: Specific energy loss as a function of momentum for different particle species in the TPC for pp collisions. The black lines indicate the expected values predicted by the Bethe-Bloch formula introduced in 1.3. Figure taken from [8].

One can identify different regions for the specific energy loss distribution. The minimum of the distribution is located around $\beta\gamma \approx 3 - 4$. The particles in that region are called minimum ionizing particles (MIPs) and they can be used for detector calibration. As the momentum transfer grows with the interaction time, which is longer for slower particles, the specific energy loss rises $\propto 1/\beta^2$ for lower $\beta\gamma$. For higher $\beta\gamma$ instead, the energy loss increases in the so-called relativistic rise $\propto \ln(\beta^2\gamma^2)$. One explanation is that the transverse electric field increases due to Lorentz transformation and thus the contributions of charges from a larger distance increases. The description of the energy loss with Bethe-Bloch is valid until $\beta\gamma \approx 1000$, where radiative processes begin to dominate over ionization. For electrons with their low mass, radiative processes are relevant at lower energies already. One of these processes is Bremsstrahlung, which is the Coulomb interaction of a charged particle with the nuclei of the surrounding matter. It is characterized by the so-called radiation length x_0, which is the distance after which the energy of the electron is reduced by a factor of $1/e$.

Chapter 2

The ALICE experiment

The data used in this analysis was taken with the ALICE (A Large Ion Collider Experiment) detector, which is one of the four big experiments at the Large Hadron Collider (LHC) at the European Organization for Nuclear Research (CERN) and is further described in [7]. The LHC can accelerate protons up to an energy of 6.5 TeV resulting in a center-of-mass energy of 13 TeV and provides several collision points. ALICE is placed at one of them.

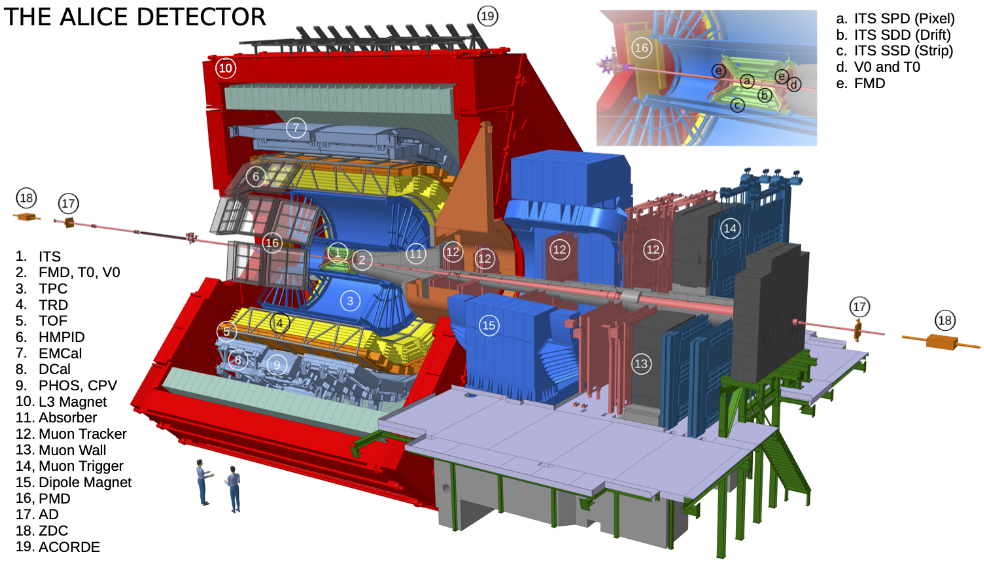

Figure 2.1: Schematic view of the ALICE detector.

The experiment is designed to measure the collisions of heavy ions in which extremely high energy densities and temperatures can occur. Besides measuring Pb-Pb collisions, ALICE takes data of pp and p-Pb collisions as well in order to have reference measurements and to test theoretical models for the production mechanism of particles. The measurement is done with an advanced system of several sub-detectors with a total dimension of 16m $\times$ 16m $\times$ 26m and an approximate weight of 10000t. The detectors are build around the interaction point where the particle collision takes place as shown in Figure 2.1. Each detector provides certain information in order to reconstruct the tracks and the energies of the produced particles and their decay products. Directly at the beam pipe, the Inner Tracking System (ITS) is located, which is a system of six layers of Silicon Pixel (SPD), Drift (SDD) and Strip (SSD) Detectors. Followed by that are the Time Projection Chamber (TPC) and the Transition Radiation Detector (TRD). All of the detectors mentioned so far, belong to the tracking system and are part of the central barrel, that is surrounded by the solenoid magnet, which is responsible for bending the tracks of charged particles. In the following the detectors that are most relevant for this study are introduced in further detail.

2.1 Silicon Pixel Detector

The SPD which is further explained in [13] is part of the ITS. It is a detector made of two layers of silicon pixels and it is located closest to the beam pipe with an inner radius of 3.9 cm and an outer radius of 7.6 cm. The working principle is based on the creation of electron-hole pairs in semiconducting detector material when a charged particle traverses it. An electric field makes the electrons and holes travel towards the electrodes in which the detector material is placed. The resulting pulse can then be measured in an outer circuit. With its 1200 chips, the SPD is capable of fulfilling its main task of reconstructing primary and secondary vertices, e.g. of weak decays of heavy-flavor hadrons. These are the points where the particles are created or where they decay.

2.2 Time Projection Chamber

The TPC that is described in [12] is the main tracking detector of the central barrel. Together, the central barrel detectors provide information about the momentum of charged particles with good two-track separation as well as particle identification and vertex determination. The TPC is a gas detector filled with a mixture of $Ne/CO_2/N_2$ (90/10/5). It has a cylindrical shape with an electrode along the symmetry axis and is covered by Multi-Wire Proportional Chambers (MWPC) that are arranged in 18 sections around the end-plates. When a charged particle traverses the TPC, it ionizes the gas molecules inside of it. Those primary electrons move towards the MWPC where the signal gets amplified and is read out by the Front End Electronics. One of the main purposes of the TPC is the particle identification (PID) which is done by measuring the specific energy loss $\mathrm{d}E/\mathrm{d}x$ with a resolution better than 10% as a function of the particle momentum with a resolution better than 2.5% for electrons with momentum of about 4 GeV/c according to [6]. The measured energy loss can be compared to the theoretical values described by the Bethe-Bloch formula and therefore be used to identify the particle.

2.3 Transition Radiation Detector

The TRD which is described in [3] is located around the TPC as shown in Figure 2.1. Its purpose is to differentiate between electrons and hadrons for intermediate and high momenta. It helps to identify electrons and to trigger on them. The detector is arranged in 18 supermodules with five stacks of six tracking chambers each. Every chamber consists of polypropylene fibre mats sandwiched between two Rohacell foam sheets as radiator material and a drift chamber behind as shown in Figure 2.2. A characteristic property of the materials is the refraction index $n = \sqrt{\varepsilon\mu}$, where ε is the relative permittivity and μ is the relative permeability. When a highly relativistic particle with Lorentz factor γ transitions from one material to another with different electric properties, transition radiation is emitted when the particle exceeds the threshold of $\gamma \approx 800$. The photon yield per boundary crossing is in the order of the electromagnetic coupling constant $\alpha = 1/137$, which is why many boundaries are needed. The produced measurable photon in the X-ray region has a large conversion probability at the beginning of the drift region due to the high-Z counting gas. Since the mass of an electron is so low, it is a lot more likely for the electron to reach the threshold Lorentz factor than it is for other particles. In addition to that, the traversing particle also interacts with the detector gas of the drift chamber and produces ionization electrons, which can be used to measure the energy loss $\mathrm{d}E/\mathrm{d}x$. All electrons drift towards the anode wires where the signal is amplified and then measured by cathode pads. Therefore, electrons and hadrons can be discriminated first by their different energy losses due to ionization, which are described by the Bethe-Bloch formula and second by the large signal for electrons at higher drift time that correspond to the region at the beginning of the drift chamber which comes from the conversion of transition radiation as depicted in Figure 2.2. The TRD is used as a trigger as explained further in Chapter 3.

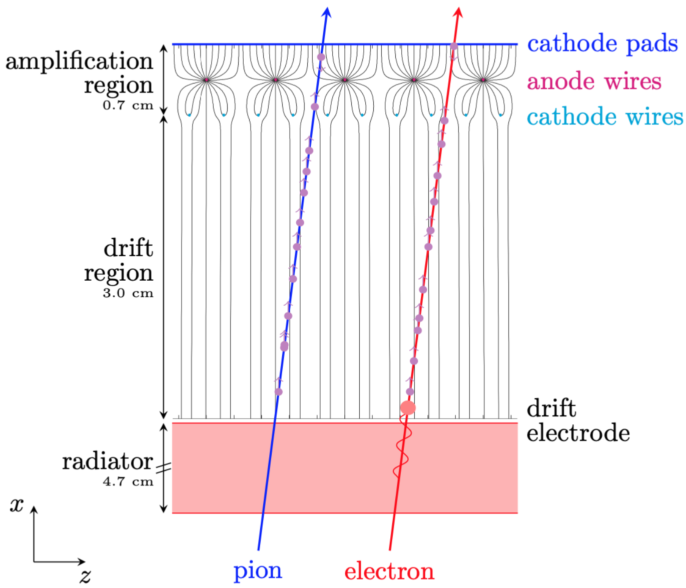

Figure 2.2: Schematic cross section of a TRD chamber in the *x*-*z* plane (perpendicular to the wires) with tracks of a pion and an electron to illustrate the ionisation energy deposition and the TR contribution. The large energy deposition due to the TR photon absorption is indicated by the large red circle in the drift region [3].

Chapter 3

Data Sample

The analysis is based on data taken by the ALICE experiment in pp collisions at $\sqrt{s} = 13$ TeV in the years 2017 and 2018. It is performed on so-called dst tree files [1]. To reduce the amount of data, files are generated from the reconstructed data that only include the information that is needed for the analysis of interest. The data taking periods which are periods where the outer conditions of the beam and the experiment are identical, of 2017 are all pass1 reconstructions, while for 2018 all periods are pass2 reconstructions, except for LHC18g, LHC18h, LHC18k, where the pass1 reconstruction is used. One run comprises data that is taken until either one of the main detectors crashed or until there is no more beam in the pipe. In total, about 126 million events are analyzed. An overview of the analyzed data set is given in Table 3.1 where the number of runs and number of events are listed. Periodwise number of runs and events can be found in Appendix A. The run selection requires that the run was ongoing for at least 10 minutes in the physics run type (pp collisions) and that information of SPD, TPC and TRD as readout detectors and of the TRD as trigger detector are available.

	N_{runs}	$N^{\text{TRD}}_{\text{events}}$	$N^{\text{TRD}}_{\text{evts.,MC}}$
LHC17[g-r]	700	$3.93 \cdot 10^7$	$4.55 \cdot 10^7$
LHC18 pass 1	18	$2.79 \cdot 10^6$	$3.08 \cdot 10^5$
LHC18 pass 2	624	$8.35 \cdot 10^7$	$4.78 \cdot 10^6$
TOTAL	1342	$1.26 \cdot 10^8$	$5.06 \cdot 10^7$

Table 3.1: Number of runs and events before the physics selection for the selection of good runs for data and MC periods used in the analysis.

During data taking, an electron trigger is operated. The TRD triggered events correspond to events that are triggered by HQU as explained in [3]. The trigger applies a cut online on the transverse momentum p_T, the PID value, which is a likelihood and results in an ”electron efficiency”, the minimum number of TRD tracklets and the saggita to reduce the number of later conversions. Further, it requires a hit in the first layer. The trigger settings are given in Table 3.2.

Criterion	HQU trigger
p_T threshold	2 GeV/c (2 GeV/c)
PID value	130 (164)
Minimum number of TRD tracklets per track	5 (5)
Sagitta cut	0.2 c/GeV (not applied)
Tracklet in Layer 0	required (applied)

Table 3.2: Conditions of the TRD electron trigger. The values in parentheses are the conditions for MC.

The values for p_T and PID are calculated online in the global tracking unit (GTU) as explained in [7]. In Figure 3.1, one can see the distribution of PID values for electrons in dependence of the momentum for events that are triggered by the TRD as an example for one data taking period. The PID cut of 130 is visible in the according rise of entries. The reason, why entries with a lower PID value are seen nevertheless is that when the TRD is triggered, the whole event is saved including other electrons with a lower PID value. The same argument is true for entries with a momentum lower than 2 GeV/c. The sagitta cut which is explained in [18] reduces the number of background electrons from photon conversions shortly before or within the TRD. It is not implemented in MC simulations. For the quality assurance and the signal extraction, only events with the flag HQU are considered.

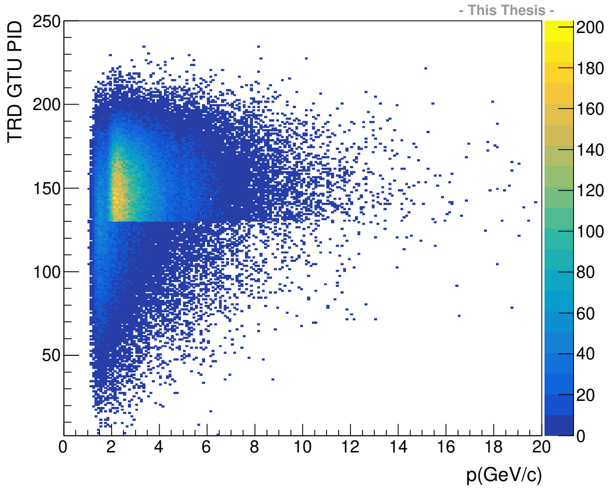

Figure 3.1: TRD GTU PID value vs momentum p for pp collisions at $\sqrt{s} = 13$ TeV for electrons in data taking period LHC18m.

3.1 Event Selection

Only events with good collision candidates, i.e. events where a beam crossing actually took place are considered for further analysis. From the recorded pp collisions, only events surviving the physics selection are included. No bias is introduced to the measurement from in-bunch pileup in minimum bias events from 2016 and 2017 according to [15]. Therefore, we can assume that the contribution of pile-up is negligible in our data. Further, the position of the primary vertex in the beam direction has to be within 10 cm from the nominal center of the ALICE experiment to ensure that the selected events are within the geometrical acceptance of the central barrel. In addition, the vertex reconstructed with hits in the SPD and the primary vertex from tracks reconstructed with ITS and TPC with at least one contributor have to be provided for all events. The difference of the two vertex reconstruction algorithms in the direction of the beam has to be smaller than 0.5 cm and the resolution in the z-position of the SPD vertex has to be smaller than 0.25 cm. The number of events after cuts are shown in Table 3.3 and periodwise in appendix A.

reconstruction	$N_{\text{events}}^{\text{before}}$	$N_{\text{events}}^{\text{after}}$	Ratio
TRD	$1.26 \cdot 10^8$	$1.23 \cdot 10^8$	0.976

Table 3.3: Number of events before and after event and physics selection.

3.2 Track Selection

The J/ψ is reconstructed from its decay channel into an electron-positron pair. The tracks of those are reconstructed in the ITS, the TPC and the TRD. In order to select good tracks for our analysis, the requirements listed in Table 3.4 must be fulfilled.

Variable	cut value
$\|\eta\|$	< 0.84
require SPD any	yes
require ITS refit	yes
$\|DCA_{xy}\|$	< 1.0 cm
$\|DCA_z\|$	< 3.0 cm
$N^{\mathrm{TPC}}_{\mathrm{clusters}}$	$\in [70, 160]$
require TPC refit	yes
χ^2_{TPC} per cluster	< 4
reject kink daughters	yes
p_T	> 1 GeV/c
χ^2_{ITS} per cluster	< 36
n_{σ_e}	$\in [-2.0, 3.0]$
n_{σ_p}	> 3.0 (> 2.0 for $p_T > 5$ GeV/c)
n_{σ_π}	> 3.0 (> 2.0 for $p_T > 5$ GeV/c)

Table 3.4: Track selection criteria.

As a kinematic cut, we require $|\eta| < 0.84$ for the pseudorapidity, even though the central barrel has an acceptance of $|\eta| < 0.9$. The reason is that the pseudorapidity coverage of the TRD is a bit smaller than that of the other detectors in the central barrel. The distribution of selected tracks in the η-φ-plane is displayed in Figure 3.2. One notices a gap of entries around $\varphi \approx 2.2$. A possible explanation is the non-operation of the SPD due to a break down of the cooling, whereby tracks traversing in that direction do not fulfill the track selection criteria. Interesting to observe is the pattern in the distribution that comes from the 18 detector sectors of the TRD in the azimuthal direction and the 5 stacks in the longitudinal direction. Both, data and MC, contain this structure and dividing them leads to an almost even allocation. Hence, MC describes the behaviour of the data well. All three histograms are scaled to their maximum entry value. In the division plot, the range of the z-axis is set to 0.4 to have a better resolution as the entries for

$\varphi \approx 3.8$ are very low for MC and thus lead to high values in the division that cause a rise in the entry-scale.

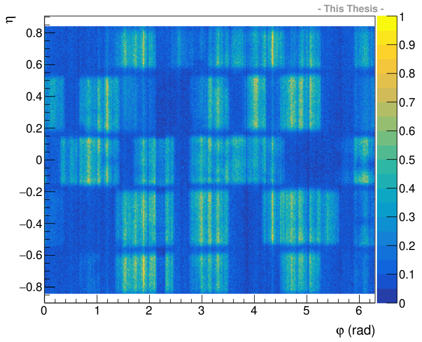

(a) Pseudorapidity η vs azimuthal angle φ for data.

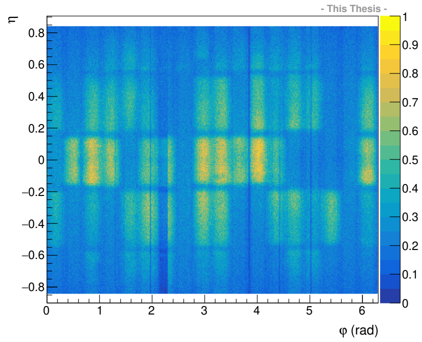

(b) Pseudorapidity η vs azimuthal angle φ for MC.

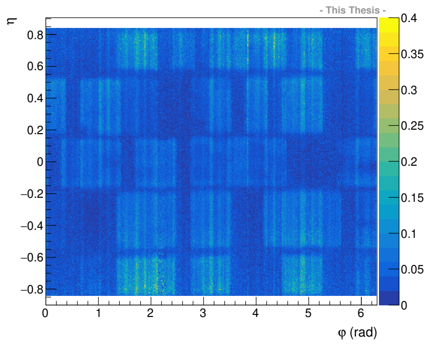

(c) Division (data/MC) of pseudorapidity η vs azimuthal angle φ.

Figure 3.2: Pseudorapidity η vs azimuthal angle φ.

Additionally, tracking cuts are applied to reject tracks from secondary particles and background sources: When a primary particle traverses the ITS, it may interact with the detector material and thereby produce secondary electrons. In order to minimize their contribution, we request SPD any, which means that the tracks must be associated with a cluster in one of the two SPD layers, which are the innermost layers of the ITS. A further improvement is done with the help of a refit in the ITS. Another observable that we apply a selection criterion on is the distance of closest approach (DCA), which is a measure for the distance of the particle tracks from the primary vertex. The applied cuts remove tracks from weak particle decays, as well as tracks, that come from material interactions with a larger displacement from the primary vertex. The quality of the reconstruction is estimated by the fraction of TPC clusters that gave a hit. The maximum number of TPC clusters is 159. We therefore demand a minimum of $N^{\mathrm{TPC}}_{\mathrm{clusters}} > 70$ for a hit to assure a good reconstruction quality. In order to remove particles that are decay products, kinked tracks are rejected. Kinked tracks arise from a charged mother particle and a corresponding charged decay product that result in an abrupt bending of the track due to different momenta.

The cut on the minimum transverse momentum of the electron candidates is done because the energy loss of electrons for momenta below 1 GeV/c has several overlap regions with the energy losses of other particles which leads to a higher background. A further improvement is done by limiting the χ^2 of the ITS to assure a good track reconstruction. Finally, we make use of the particle identification of the TPC and demand an electron inclusion by limiting the n_σ which is defined in 4.1 to values between -2.0 and 3.0 around the expected energy loss. At the same time, proton and pion candidates are rejected by requiring n_{σ_p} and $n_{\sigma_\pi} > 3$ or > 2 depending on the momentum-interval. For higher momenta (above 5 GeV/c), a looser cut is applied to not reject electrons together with hadrons in the relativistic rise, whose energy loss becomes more similar to that of electrons. Thus, the signal loss is kept low. Several cuts, namely the cuts on p_T, ITS χ^2 and the PID-values were not applied for the particle identification as we wanted to increase the sample size for that.

3.3 Monte Carlo Simulation

In order to obtain the required signal shape for the signal extraction we use Monte Carlo (MC) samples. The different data taking periods and their corresponding number of events can be seen in Table 3.1. The samples are generated using the simulation program PYTHIA [19] reflecting a realistic particle transport and detector performance for each run. On top of each event one J/ψ is injected. The injections are done as 70% prompt J/ψ that follow a "natural" p_T spectrum for $p_T > 0$ GeV/c and a flat spectrum for $p_T > 6$ GeV/c to enrich the amount of high-p_T particles. The other 30% are injected as non-prompt J/ψ that originate from B hadrons which are forced to decay into J/ψ. The simulation for that is also included in PYTHIA. The decay of J/ψ in the dielectron channel including the full QED radiative decay is carried out with PHOTOS [21]. More details on the MC samples can be found in the corresponding JIRA ticket (ALIROOT-7416). The TRD trigger simulation is implemented in the MC simulation.

3.4 V0 Particles

For the calibration of the particle identification of the TPC, the physics sample is not the most suitable choice due to its high background coming from hadron contamination. Instead, decay products of so-called V0 particles can be used since that leads to a purer sample. An advantage of that is the fact that the PID can be done based on a decay topology that does not rely on the energy loss $\mathrm{d}E/\mathrm{d}x$ measured in the TPC. V0 particles are heavy, unstable, subatomic particles with a neutral electric charge. They can decay into two daughter particles with opposite electric charge via weak decay. They were first observed in bubble chambers and the V0 particles themselves as neutral particles were not visible but the two charged daughter particles that appeared in a V-shape were.

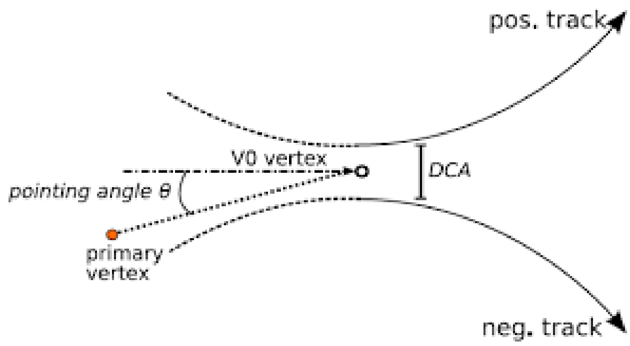

Figure 3.3: Topology of a V0 decay. Figure taken from [10].

The most frequent V0 particles are Λ baryons and K_S^0 mesons. The Λ baryons decay into a p and a π and can therefore be used for the p-calibration, the K_S^0 mesons decay into two pions and are hence used for the π-calibration. Identifying those V0 particles is implemented in AliRoot as explained in [10] by applying several selection criteria, e.g:

- Distance of the daughter tracks to the primary vertex
- Distance of closest approach (DCA) between the daughter tracks
- Pointing angle θ (momentum of mother particle should point to the primary vertex)

The exact cut values depend on the type of V0 particle that one is interested in and can be found in [10].

Not only the decay of a V0 particle into its charged daughter particles can be identified like that but also the photon conversion into an e^+e^- pair when interacting in matter. This can be used for the electron calibration.

Chapter 4

Particle Identification

For analyzing the J/ψ production, we use the decay channel into electrons. Therefore, we need to identify electrons correctly and get their momentum in order to reconstruct the invariant mass of the mother particle. The particle identification (PID) is done using the TPC. The energy loss of a traversing particle in the TPC is measured and compared to the theoretical value predicted by Bethe-Bloch. We then have a look at the difference of the the theoretical value and the experimental value:

$$n_\sigma = \frac{\langle dE/dx \rangle_{\text{measured}}(trk) - \langle dE/dx \rangle_{\text{expected}}(trk)}{\sigma_{TPC}(trk)}. \tag{4.1}$$

Here σ_{TPC} is the detector resolution. We thus get the standard deviation of the particle energy loss with respect to the theoretical value. In Figure 4.1, one can see the entries of n_σ in dependence of the momentum p for a subset of the whole data set. The colors represent the number of entries in each bin from blue with the least amount of entries up to yellow with the highest amount of entries. The entries around $n_\sigma \approx 0$ are what we can identify as electrons. The values are taken from the tree-file, to which a loose hadron-rejection is already applied in order to reduce the amount of contamination. The yellow peak at $n_\sigma \approx -5$ can be explained by hadrons that have a similar energy loss in the low-p-region. The increase in yellow color at $n_\sigma \approx -2$ can be explained by pions, which start with the relativistic rise. Most of them are cut out in the hadron rejection when filling the trees, which explains the edge. The rejection is also visible at $p \approx 1$ GeV/c, where the energy loss of the proton crosses that of the electron, which makes it difficult to distinguish between background and signal and hence a cut is applied. In fact, not all hadrons are cut out to not lose too much of the signal, but the impact of this contamination is negligible as the hadrons do not recombine to the invariant mass of J/ψ.

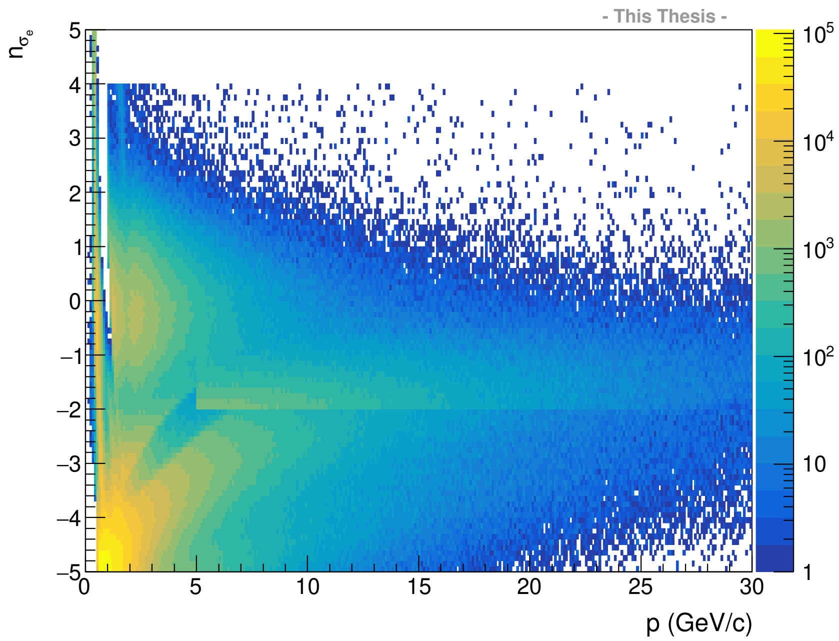

Figure 4.1: TPC n_σ vs momentum p of electrons triggered by the TRD as an example for data taking period LHC18m.

For the purpose of analyzing the electron candidates, we project the above distribution onto n_σ in steps of 1 GeV/c ranging from 0 GeV/c up to 20 GeV/c. An example for that can be seen in Appendix C.1. A Gaussian distribution is fitted to the projection for the signal and an exponential decay for the background. One can already notice here that for higher momenta it is not sufficient anymore to distinguish between signal and background. The reason for that is the low statistics for higher momenta and the lower separation power that is due to the relativistic rise of the hadrons. The mean is not located at $n_\sigma \approx 0$ as shown in Appendix C.1 and as one would expect for a pure electron distribution, which is due to the calibration of the TPC. We hence need to determine correction values to improve the data by applying a post-calibration.

The same kind of analysis is done with n_σ in dependence of the pseudorapidity η. Here the projection onto n_σ is done in steps of 0.1 ranging from -0.9 up to 0.9. One has to note here that the TRD covers a range of $-0.84 < \eta < 0.84$ and thus the according cut is applied to our data which means that the first and the last bin of our projection include less entries than the bins in between. Again, a Gaussian is fitted to the signal, but no background is added to the fit, since the distribution seems pure enough. Again, the mean value differs from the expected value for a pure electron distribution of $n_\sigma \approx 0$ as shown in C.1 which we have to correct for. Since the momentum p and the pseudorapidity η are dependent variables, it is sufficient to correct for one of them, as it will also effect the other one. Therefore, we decided to correct for η as the distribution is more even and hence does not show a geometrical bias. The post calibration in η will lead to corrected results in p as well.

4.1 Correction Parameters

To compare the different data taking periods, a projection onto n_σ is done for $0\ \mathrm{GeV} < p < 4\ \mathrm{GeV}$ and the signal and background are fitted to get the mean and error for n_σ as shown in Appendix C.1. From that, one can conclude that the data taking periods from 2017 all behave similarly and do not necessarily need a correction, since their n_σ is already well calibrated. This has also been verified by analyzing n_σ for V0 samples from 2017 in [15]. In 2018, the periods that are reconstructed with pass2 behave alike, but the periods with reconstruction pass1 (LHC18g, LHC18h, LHC18k) behave differently as shown in Appendix C.1. Therefore, we decide to determine the correction parameters not period by period but instead merge data taking periods from pass 1 and those from pass2, since they show similar behavior and thus enlarge the statistics. In order to obtain the correction parameters, not the physics data is used, but instead V0 particles and photon conversions are identified for all data taking periods which have no background and therefore make the fitting more precise as there is no bias. A single Gaussian is fitted to the TPC n_σ for each particle individually in bins of η. Then the physics data is corrected the following way:

$$n_\sigma^{\mathrm{calib}}(\eta) = \frac{n_\sigma(\eta) - n_0(\eta)}{w(\eta)} \tag{4.2}$$

Here n_0 stands for the mean of the V0 sample, w for its width and n_σ for the mean value before the correction.

4.2 Post-Calibrated TPC n_σ

In Figure 4.2, the mean values for the TPC n_σ before (left) and after (right) the post-calibration for electrons vs the momentum p (top) and pseudorapidity η (bottom) of the V0 sample from 2018 are displayed. The reconstructions for pass1 and pass2 are plotted separately since different calibrations are applied to them. The slight shift in the p/η-direction for pass2 is for better visibility of both results. We only plot the mean values for p-intervals that exceed a certain entry-threshold. The same corrections are applied to the physics sample triggered by the TRD. The result can be seen in Figure 4.3.

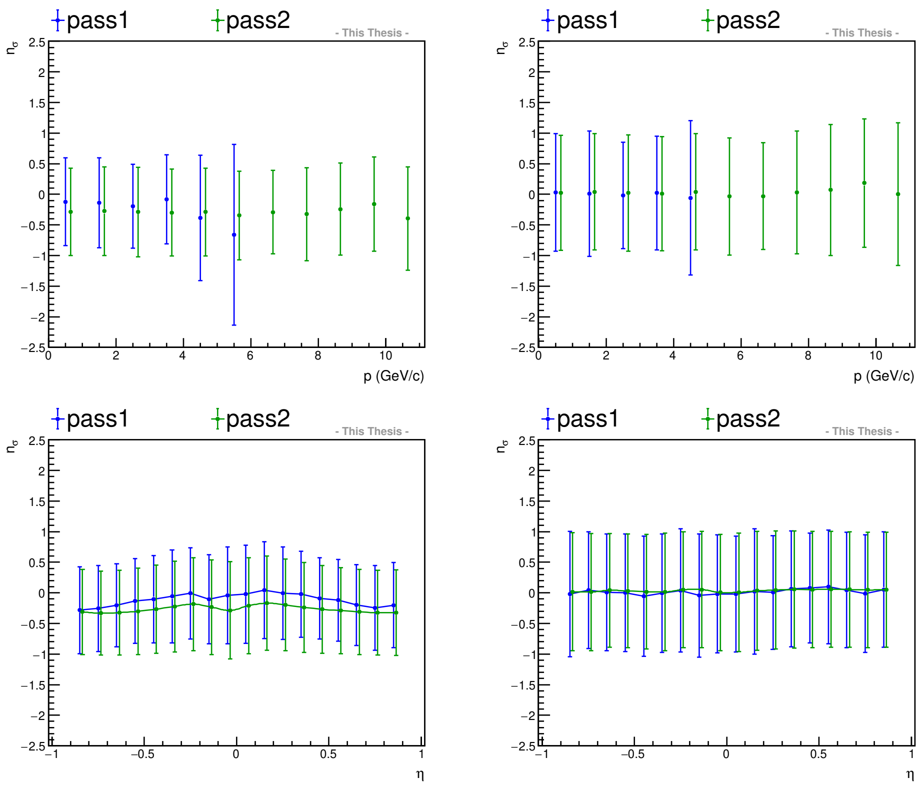

Figure 4.2: Mean and width of the Gaussian fit for TPC n_σ vs momentum (top) and pseudorapidity (bottom) for electrons from photon conversion processes in the LHC18 pass1 and pass2 reconstruction before (left) and after (right) the correction.

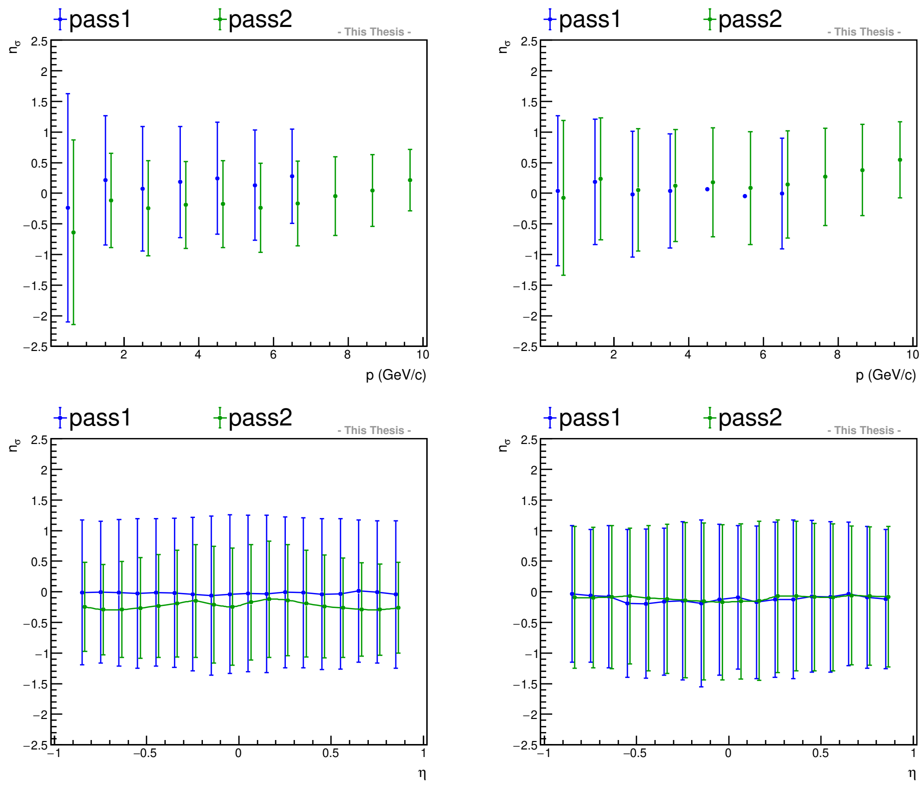

Figure 4.3: Mean and width of the Gaussian fit for TPC n_σ vs momentum (top) and pseudorapidity (bottom) for electrons triggered by the TRD in the LHC18 pass1 and pass2 reconstruction before (left) and after (right) the correction.

After the post-calibration procedure, the mean values of n_σ are centered around 0 with a width of approximately 1 for both, the momentum p and the pseudorapidity η. The post-calibration was done for the TPC n_σ of protons and pions as well accordingly for a better hadron rejection. The results can be found in Appendix C.1.1.

Chapter 5

Quality Assurance

In order to check, whether the behaviour of data is reasonable and well described by the MC simulation, a quality assurance (QA) needs to be done. From that, one can conclude, whether an exclusion of a data set is required or the inclusion in further analysis, i.e. the signal shape, is reasonable.

5.1 Runwise Event Quality Assurance

The quality assurance for several quantities concerning the event quality is done runwise to account for different outer conditions. For these checks, the event selection criteria described in Section 3.1 are applied. In each QA plot, the values for MC, which are all pass1 reconstructions, are shown, as well as for the data where pass1 and pass2 reconstructions are displayed in different colors to see whether they reveal any differences between the two. In Figure 5.1, the average position of the primary vertex in the z-direction is shown. It is centered around 0 cm which indicates that the collision takes place symmetrically. The high errors which are the widths of the Gaussian fits of the vertex position distributions for the earlier runs are due to the low number of events for those periods. Additionally, plots for the average number of SPD tracklets, the average vertex position in x- and y-direction can be found in Appendix C.2. All of them show a stable tendency with values as expected and a good representation in MC.

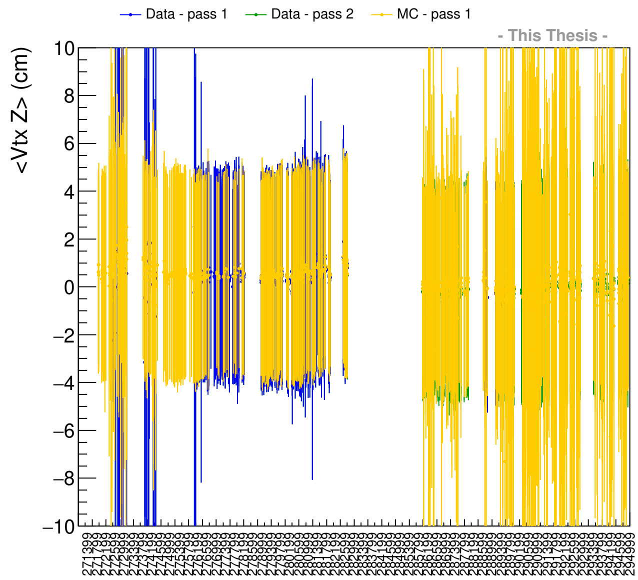

Figure 5.1: Average position of the z-vertex for accepted events vs run number. The labels along the x-axis show the run number for every 400th run.

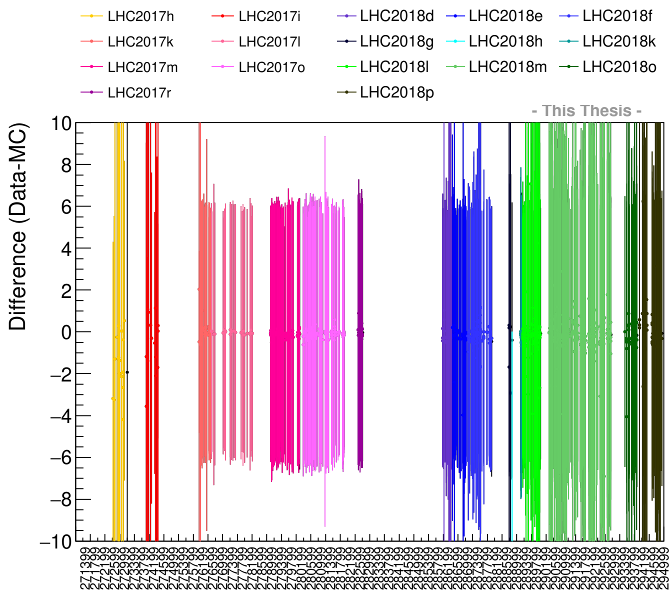

Figure 5.2: Difference (data-MC) of the average position of the z-vertex for accepted events vs run number. The labels along the x-axis show the run number for every 400th run.

In order to quantify how well the MC simulations describe the data, the difference or ratio of data and MC are calculated for each run, depending on the similarity of the corresponding values as shown as an example in Figure 5.2. For the comparison, the mean difference/ratio and its standard deviation are calculated and all runs that differ from the mean with more than 3σ are checked manually. It turns out that the critical runs all seem to have a small number of events which can be the reason for the larger deviation as the statistics are not high enough. Overall, a good agreement between data and MC is observed and no runs have to be excluded.

5.2 Runwise Electron Track Quality Assurance

Not only the quality of the events needs to be assured but also the quality of the tracks. One of the characteristics checked is the geometry of the tracks, i.e the angular distribution. The corresponding plots, as well as the plots for ITS-χ^2, are shown in Appendix C.3. Another quantity that is observed is the transverse momentum p_T that can be seen in Figure 5.3. One notices that the p_T-value for MC is higher than the value for the data by a factor of around 3. This can be explained by the injection of high-momentum particles in the MC-sample. The average p_T in the MC simulation for data taking period LHC17o differs from the other periods, which we have to take into consideration in the efficiency correction in the future. Period LHC17o is thus excluded from the extraction of the signal shape used in Chapter 6.

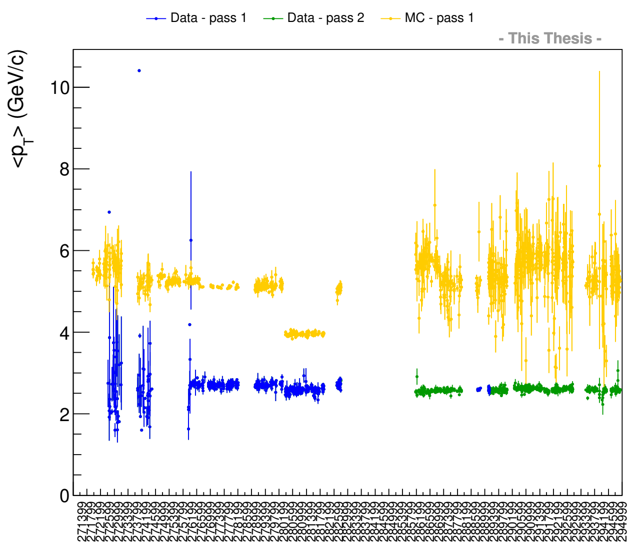

Figure 5.3: Average transverse momentum p_T vs run number. The labels along the x-axis show the run number for every 400th run.

The average value for the DCA in the x-y-plane and in the z-direction for the data and for MC can be seen in Figure 5.4.

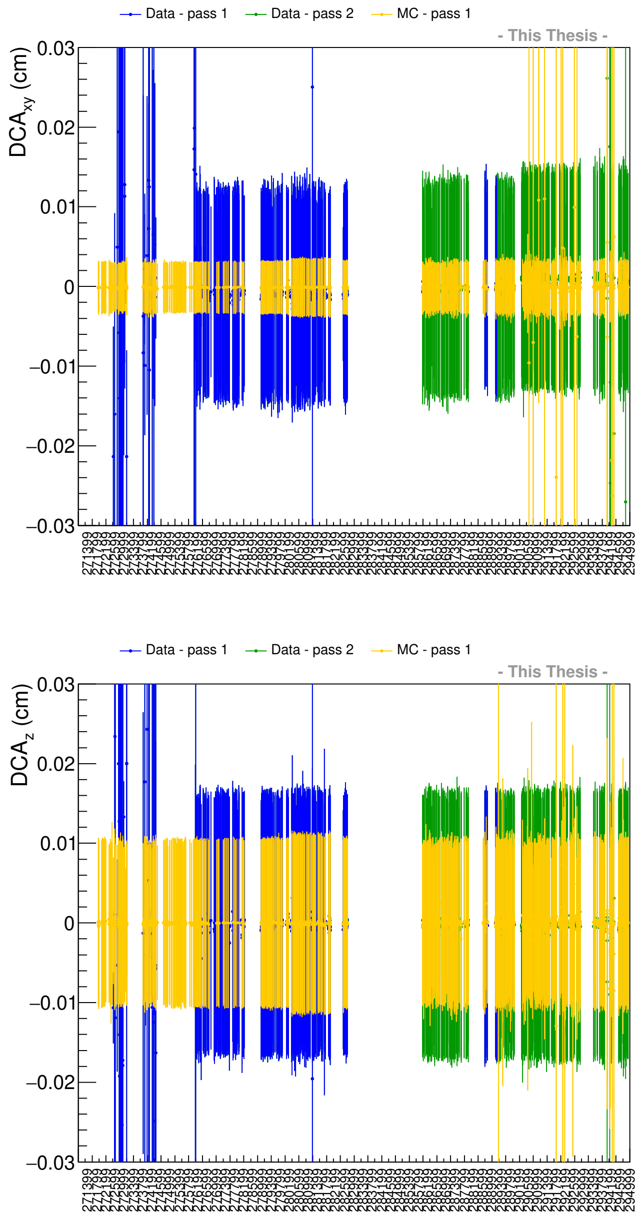

Figure 5.4: Average DCA in the x-y-plane (top) and the z-plane (bottom) for data and MC. The labels along the x-axis show the run number for every 400th run.

The average number of clusters in the ITS is shown in 5.5. One notices that the mean value for MC is higher than the one for the data. This can be explained by the fact that the composition of particles and the particle abundances are different in MC as J/ψ mesons are injected. J/ψ mesons generate two hard primary electrons which have more ITS clusters per track. Thus, the average number of ITS clusters for MC is raised.

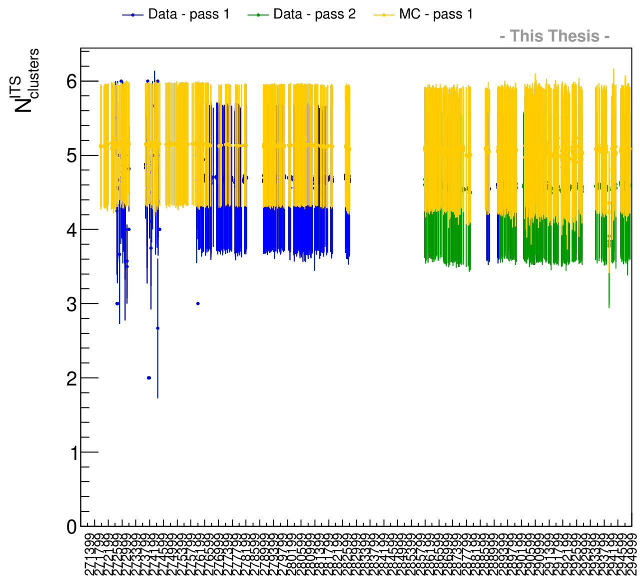

Figure 5.5: Average number of ITS clusters vs run number. The labels along the x-axis show the run number for every 400th run.

In Figure 5.6, the mean number of TPC clusters is displayed. Again, the entries for MC show a higher mean out of the same reasoning. Since the cut on TPC clusters is not tight, this will not affect the further analysis.

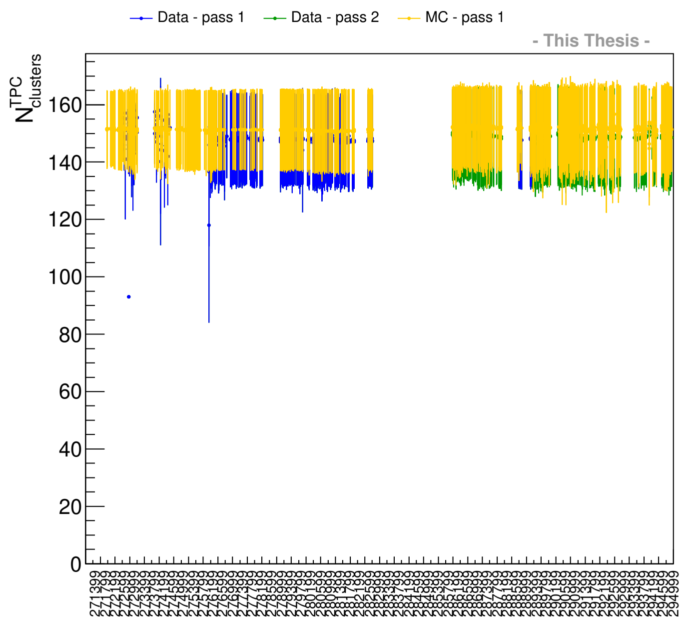

Figure 5.6: Average number of TPC clusters vs run number. The labels along the x-axis show the run number for every 400th run.

In Figure 5.7, one can see the average TPC n_σ for the V0 sample of electrons after the applied post-calibration for 2018. It shows an average value of approximately 0 and a width of around 1 as expected for a pure electron distribution.

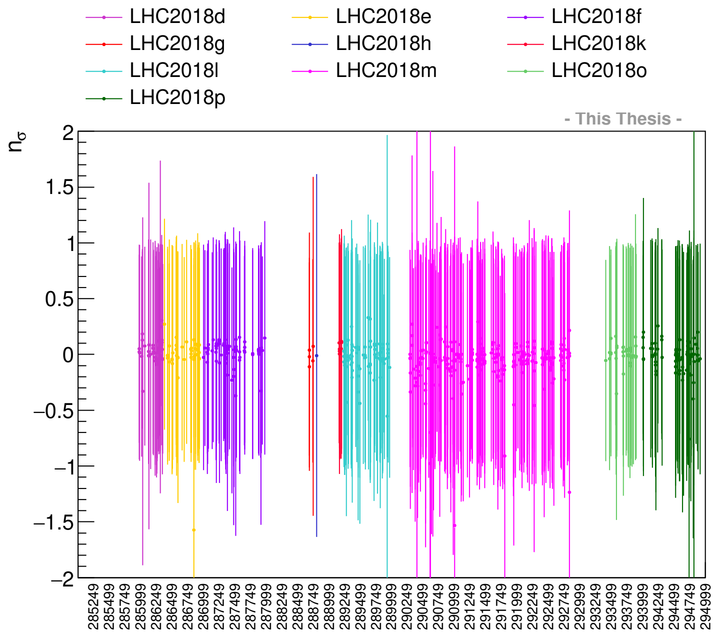

Figure 5.7: Average TPC n_σ vs run number for the V0 samples of 2018. The labels along the x-axis show the run number for every 250th run.

From the QA, one can conclude that there is a good agreement between data and MC for quantities concerning the quality of tracks and no run has to be excluded from the data analysis. The whole MC sample besides data taking period LHC17o can be used to obtain the J/ψ signal shape.

Chapter 6

J/ψ Signal Extraction

The extraction of the J/ψ signal is done by combining all electron-positron-candidates from mixed events to pairs, subtracting the estimated background and counting the bins in the signal region of the invariant mass distribution of the mother particle. The signal is extracted for several p_T intervals to obtain the uncorrected differential yield.

6.1 Pair Selection

Electrons and positrons fulfilling the selection criteria described in Section 3.2 are combined to e^+e^- pairs and their invariant mass distribution can be used for the signal extraction. Most of those pairs are background not originated from J/ψ decays. The background is composed of pairs which do not have a common physical source, so-called uncorrelated background and pairs from correlated backgrounds, i.e. from jet fragmentations or decays of heavy-flavor hadrons. One needs to subtract the background from the invariant mass distribution in order to obtain a clear J/ψ signal. There are several methods to estimate the background. In this analysis the so-called hybrid signal extraction method is used which determines the uncorrelated and the correlated background separately as also done in [22].

6.2 Hybrid Signal Extraction Method

The hybrid signal extraction method is a two-step procedure: The uncorrelated background is estimated by using pairs with legs from different events, whilst the correlated background is estimated with the help of a fit function.

The first step is the subtraction of the uncorrelated background, which is obtained from unlike-sign (US) pairs taken from mixed events (ME). For ME an event pool of 100 events is used, where only events within a certain category[1] are mixed to ensure that they consist of comparable events and similar geometrical acceptance. The ME-US distribution is then scaled in the region $2 < m_{\mathrm{inv.},e^+e^-} < 5$ GeV/c^2 excluding the range $2.5 < m_{\mathrm{inv.},e^+e^-} < 3.2$ GeV/c^2 of the signal. This is done by using the corresponding like-sign (LS) distributions of pairs from the same event (SE) and from ME, consisting of e^+e^+ and e^-e^- pairs, and taking their ratio (SE-LS)/(ME-LS). The estimation for the background using ME can be seen in red in the upper panel of Figure 6.1.

The second step is the estimation of the correlated background by using a fit function. The signal is characterized by a tail towards lower invariant mass that comes from the energy loss of electrons and positrons via Bremsstrahlung. In order to get a better result for the fit, the shape of the tail is determined with the help of the J/ψ signal shape from MC. The fit-function, represented by the dashed black line in the lower panel of Figure 6.1, is the sum of the MC template and a second order polynomial, which leads to a continuous background. For MC the samples of all data taking periods besides LHC17o are used as explained in Chapter 5.

After the subtraction of both background contributions, the signal is obtained by counting the bins in the invariant mass window $2.921 < m_{\mathrm{inv.},e^+e^-} < 3.159$ GeV/c^2.

6.3 Uncorrected p_T-Integrated J/ψ Signal

The extraction of the uncorrected p_T-integrated J/ψ signal can be seen in Figure 6.1. For that, J/ψ mesons with a momentum greater than 2 GeV/c are counted since lower momentum J/ψ mesons are very unlikely due to the selection criterion on the transverse momentum of electrons triggered by the TRD.

[1] The events are categorized according to their position of the z-vertex (−10., −8., −6., −4., −2., 0., 2., 4., 6., 8., 10.) and their average number of SPD tracklets (1., 15., 25., 35., 45., 55., 65., 80., 110., 150., 400.).

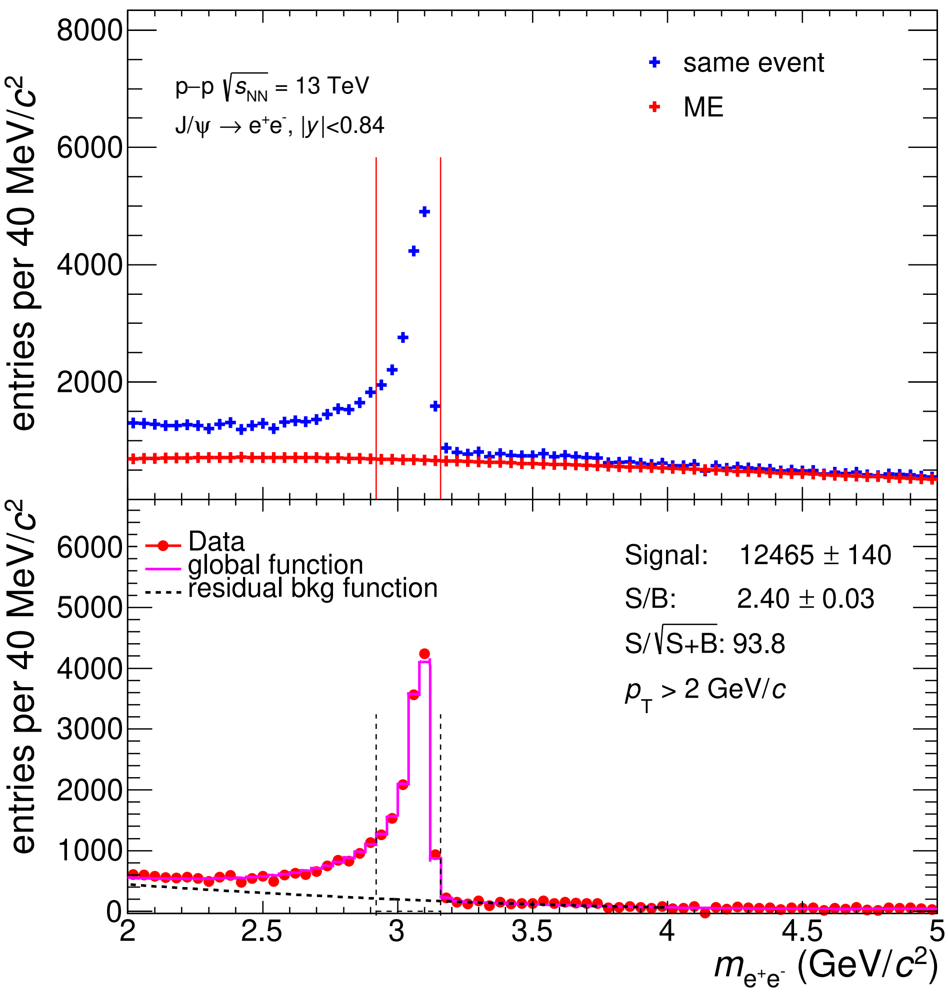

Figure 6.1: Invariant mass distribution of e^+e^- pairs with the uncorrelated background in red in the top panel and after subtraction of the uncorrelated background with the fit for the correlated background in black and the MC signal in pink in the lower panel. The invariant mass window in which the signal was counted is shown in both panels.

In the top panel, the invariant mass distribution can be seen together with the uncorrelated background for the p_T-integrated case in the pseudorapidity range $|\eta| < 0.84$. The lower panel shows the distribution of the invariant mass after the subtraction of the uncorrelated background, the fit function for the correlated background as well as the global fit function. Also, the invariant mass window used for counting the signal is drawn in. The obtained integrated uncorrected $J\psi$ signal yields 12465 ± 140.

6.4 Uncorrected p_T-Differential J/ψ Signal

The signal extraction for the p_T intervals of $6-7$ GeV$/c$ and $16-20$ GeV$/c$ can be seen in Figure 6.2 as examples.

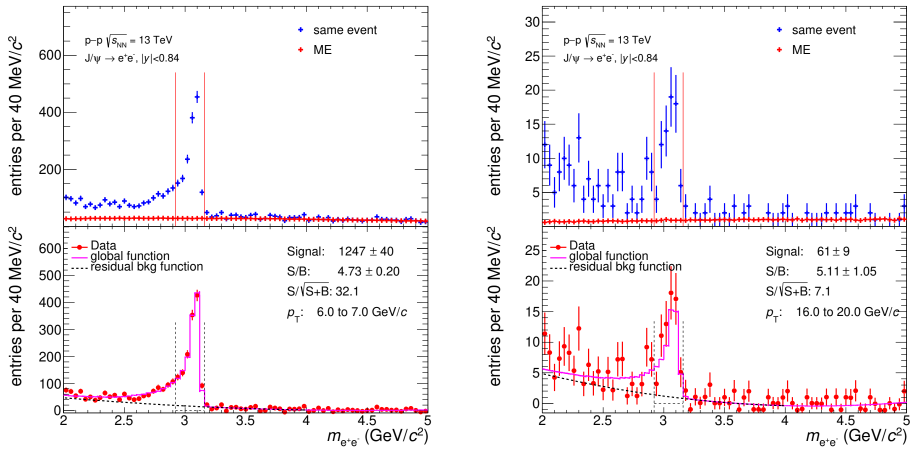

Figure 6.2: Invariant mass distribution of e^+e^- pairs for p_T bins $6-7$ GeV$/c$ (left) and $16-20$ GeV$/c$ (right) with the uncorrelated background in red in the top panel and after subtraction of the uncorrelated background with the fit for the correlated background in black and the MC signal in pink in the lower panel. The invariant mass window in which the signal was counted is shown in both panels.

In Figure 6.3, the uncorrected p_T-differential J/ψ signal is plotted in steps of 1 GeV$/c$ for low momenta, steps of 2 GeV$/c$ for intermediate momenta above 10 GeV$/c$ and steps of 4 GeV$/c$ for higher momenta above 16 GeV$/c$. The first bin ($2-3$ GeV$/c$) is lower caused by the TRD excluding low momentum electrons from the analysis and us applying a p_T cut. These would be the corresponding daughter particles of a low momentum J/ψ. One has to account for that in the efficiency. The signal to background ratio S/B for each p_T-bin is shown in Figure 6.4. The ratios are determined in the same invariant mass window as the signal extraction. The signal to background ratio improves for higher p_T.

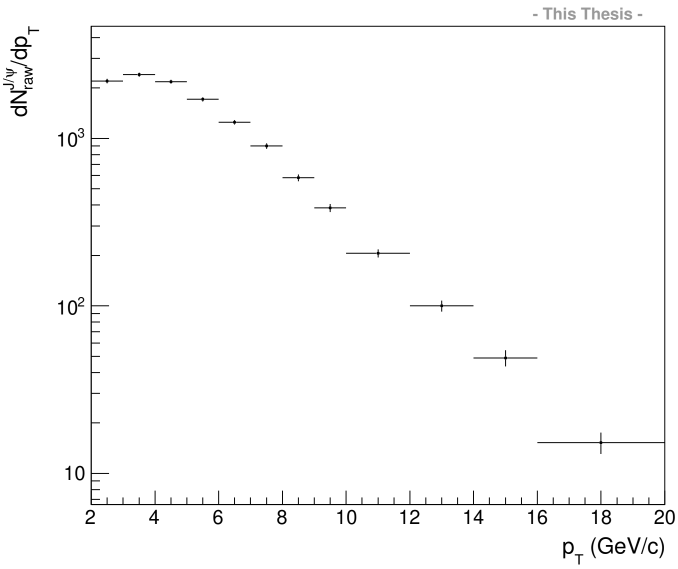

Figure 6.3: Raw differential J/ψ signal with uncertainties vs transverse momentum with bin width as bars.

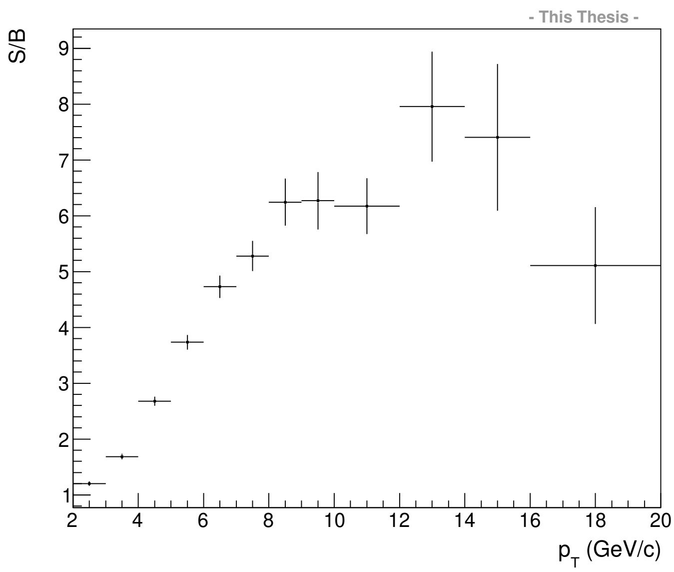

Figure 6.4: Differential signal to background ratio S/B with uncertainties vs transverse momentum with bin width as bars.

Chapter 7

Conclusion and Outlook

In this thesis, a first look at the J/ψ yield in the di-electron decay channel in pp collisions at $\sqrt{s} = 13$ TeV was presented using a high-p_T electron enriched data sample triggered by the TRD in the ALICE experiment. The electron candidates were identified by using the standard deviation of the specific energy loss $\mathrm{d}E/\mathrm{d}x$ measured by the TPC from the theoretical value predicted by Bethe-Bloch. In order to improve the identification, a correction to n_σ was done for the data taking periods of 2018, which was done separately for the reconstructions with pass1 and pass2. For that, V0 samples were used as they provide particle identification independent of the specific energy loss $\mathrm{d}E/\mathrm{d}x$. The corrections were applied separately to electrons, protons and pions. For 2017, no correction needed to be done as n_σ was well calibrated. Next, a quality assurance was done verifying whether the behaviour of the data was reasonable and was described well by MC simulations. Quantities tested for the event quality were the position of the vertex in the x-, y- and z-direction and the average number of tracklets in the SPD. All of them showed a stable tendency as a function of the run number and are in good agreement with the MC simulations. Other quantities were analyzed to ensure a good quality of the tracks, e.g. the angular distribution in η- and φ-direction, χ^2 for the tracking fits of the ITS, the transverse momentum p_T, the average DCA in the z- direction, as well as in the $x-y$-plane, the number of clusters that gave a hit in the ITS and the number of clusters of the TPC. One other quantity studied was the value for the TPC n_σ for electrons after the corrections for 2018. The quantities above all showed a stable tendency over the different run numbers and are described well by MC. The MC sample for LHC17o showed a discrepancy for the transverse momentum and was therefore excluded from the signal shape extraction. Finally, the uncorrected signal of J/ψ was obtained from the invariant mass spectrum of e^+e^- pairs from which the combinatorial background was subtracted by using the ME-US method. The correlated background was estimated by a fit with the model composed of the signal shape obtained from the MC simulation and a second order polynomial and was subtracted. The uncorrected signal was then extracted by counting bins in the invariant mass window $2.921 < m_{\mathrm{inv.},e^+e^-} < 3.159$ GeV/c^2 resulting in 12465 ± 140 counts for $p_T > 2$ GeV/c. For more detailed analysis, the uncorrected signal of J/ψ and the signal to background ratio were also analyzed differential by counting bins in certain p_T-intervals.

To complete this analysis, one has to take the acceptance and efficiency into account with the help of MC simulations. These can be used to correct the raw J/ψ signal and obtain the actual J/ψ yield and cross section. In addition, the different contributions to the systematic uncertainty need to be determined. Subsequently, one can use the obtained J/ψ yield for testing theoretical predictions for the production mechanism of J/ψ and as a reference for measurements in heavy-ion collisions.

Appendix A

Periodwise Run and Event Number

Data taking period	N_{runs}	$N_{\text{events}}^{\text{before}}$	$N_{\text{events}}^{\text{after}}$	Ratio	$N_{\text{events}}^{\text{MC}}$
LHC17h	113	$1.66 \cdot 10^5$	$1.62 \cdot 10^5$	0.975	$7.80 \cdot 10^6$
LHC17i	42	$3.91 \cdot 10^3$	$3.80 \cdot 10^3$	0.971	$2.91 \cdot 10^6$
LHC17k	115	$2.49 \cdot 10^6$	$2.44 \cdot 10^6$	0.980	$1.10 \cdot 10^7$
LHC17l	127	$1.41 \cdot 10^7$	$1.38 \cdot 10^7$	0.981	$3.96 \cdot 10^6$
LHC17m	102	$1.15 \cdot 10^7$	$1.13 \cdot 10^7$	0.977	$7.27 \cdot 10^6$
LHC17o	171	$8.75 \cdot 10^6$	$8.53 \cdot 10^6$	0.975	$1.00 \cdot 10^7$
LHC17r	30	$2.33 \cdot 10^6$	$2.26 \cdot 10^6$	0.972	$2.55 \cdot 10^6$
LHC18d	46	$6.86 \cdot 10^5$	$6.64 \cdot 10^5$	0.967	$4.07 \cdot 10^5$
LHC18e	43	$1.14 \cdot 10^6$	$1.12 \cdot 10^6$	0.977	$6.32 \cdot 10^5$
LHC18f	75	$6.56 \cdot 10^6$	$6.35 \cdot 10^6$	0.969	$6.42 \cdot 10^5$
LHC18g	6	$9.66 \cdot 10^5$	$9.33 \cdot 10^5$	0.966	$2.27 \cdot 10^5$
LHC18h	1	$6.86 \cdot 10^5$	$6.64 \cdot 10^5$	0.967	$2.52 \cdot 10^4$
LHC18k	11	$1.14 \cdot 10^6$	$1.12 \cdot 10^6$	0.977	$5.56 \cdot 10^4$
LHC18l	85	$1.33 \cdot 10^7$	$1.31 \cdot 10^7$	0.980	$6.48 \cdot 10^5$
LHC18m	260	$4.53 \cdot 10^7$	$4.40 \cdot 10^7$	0.970	$1.48 \cdot 10^6$
LHC18o	36	$6.56 \cdot 10^6$	$6.35 \cdot 10^6$	0.969	$3.57 \cdot 10^5$
LHC18p	79	$9.98 \cdot 10^6$	$9.71 \cdot 10^6$	0.973	$6.09 \cdot 10^5$

Table A.1: Number of runs, number of events before and after event and physics selection, the ratio of these and number of events for MC.

Appendix B

Runlist

LHC17h

271868, 271870, 271871, 271873, 271874, 271878, 271879, 271880, 271881, 271886, 271908, 271911, 271912, 271915, 271921, 271925, 271946, 271953, 271955, 271962, 271969, 271970, 272020, 272025, 272029, 272034, 272036, 272038, 272039, 272040, 272041, 272042, 272075, 272076, 272100, 272101, 272123, 272151, 272152, 272153, 272154, 272155, 272156, 272194, 272335, 272340, 272359, 272360, 272388, 272389, 272394, 272395, 272400, 272411, 272413, 272414, 272417, 272461, 272462, 272463, 272466, 272468, 272469, 272521, 272574, 272575, 272577, 272585, 272607, 272608, 272610, 272620, 272691, 272692, 272746, 272747, 272749, 272760, 272762, 272763, 272764, 272782, 272783, 272784, 272828, 272829, 272833, 272834, 272835, 272836, 272870, 272871, 272873, 272880, 272903, 272905, 272932, 272933, 272934, 272935, 272939, 272947, 272949, 272976, 272983, 272985, 273009, 273010, 273077, 273099, 273100, 273101, 273103

LHC17i

273824, 273825, 273885, 273886, 273887, 273889, 273918, 273942, 273946, 273985, 273986, 274058, 274063, 274064, 274092, 274094, 274125, 274147, 274148, 274212, 274232, 274259, 274263, 274264, 274266, 274268, 274269, 274270, 274271, 274276, 274278, 274280, 274281, 274283, 274329, 274352, 274355, 274357, 274360, 274363, 274364, 274442

LHC17k

274736, 274801, 274802, 274803, 274806, 274807, 274811, 274815, 274817, 274822, 274877, 274878, 274882, 274883, 274884, 274886, 274978, 274979, 275067, 275068, 275075, 275076, 275150, 275151, 275173, 275174, 275177, 275180, 275184, 275188, 275239, 275245, 275246, 275247, 275283, 275314, 275322, 275324, 275326, 275328, 275332, 275333, 275360, 275361, 275369, 275372, 275394, 275395, 275401, 275406, 275443, 275453, 275456, 275457, 275459, 275467, 275472, 275515, 275558, 275559, 275612, 275621, 275622, 275623, 275624, 275647, 275648, 275650, 275657, 275661, 275847, 275924, 275925, 276012, 276013, 276017, 276040, 276041, 276045, 276098, 276099, 276102, 276104, 276105, 276108, 276135, 276140, 276141, 276145, 276166, 276169, 276170, 276177, 276178, 276230, 276259, 276290, 276291, 276292, 276294, 276297, 276302, 276307, 276312, 276348, 276351, 276429, 276435, 276437, 276438, 276439, 276462, 276506, 276507, 276508

LHC17l

276551, 276552, 276553, 276557, 276608, 276644, 276669, 276670, 276671, 276672, 276674, 276675, 276762, 276916, 276917, 276920, 276969, 276970, 276971, 276972, 277015, 277016, 277017, 277037, 277073, 277076, 277079, 277082, 277087, 277091, 277117, 277121, 277155, 277180, 277181, 277182, 277183, 277184, 277188, 277189, 277193, 277194, 277196, 277197, 277256, 277257, 277262, 277293, 277310, 277312, 277314, 277360, 277383, 277384, 277386, 277389, 277417, 277418, 277470, 277472, 277473, 277476, 277477, 277478, 277479, 277530, 277531, 277534, 277536, 277537, 277574, 277575, 277576, 277577, 277721, 277723, 277725, 277745, 277746, 277747, 277749, 277794, 277795, 277799, 277800, 277801, 277802, 277805, 277834, 277836, 277841, 277842, 277845, 277847, 277848, 277870, 277876, 277897, 277898, 277899, 277900, 277901, 277903, 277904, 277907, 277930, 277952, 277987, 277988, 277989, 277991, 277996, 278121, 278122, 278123, 278126, 278127, 278130, 278163, 278164, 278165, 278166, 278167, 278189, 278191, 278215, 278216

LHC17m

278959, 278960, 278963, 278964, 278999, 279000, 279005, 279007, 279008, 279035, 279036, 279041, 279043, 279044, 279068, 279069, 279073, 279074, 279075, 279106, 279107, 279117, 279118, 279122, 279123, 279130, 279155, 279157, 279199, 279201, 279207, 279208, 279234, 279235, 279238, 279242, 279264, 279265, 279267, 279268, 279270, 279273, 279274, 279309, 279310, 279312, 279342, 279344, 279348, 279349, 279354, 279355, 279391, 279410, 279435, 279439, 279441, 279483, 279487, 279488, 279491, 279550, 279559, 279630, 279632, 279641, 279642, 279676, 279677, 279679, 279682, 279683, 279684, 279688, 279689, 279715, 279718, 279719, 279747, 279749, 279773, 279826, 279827, 279830, 279853, 279854, 279855, 279879, 279880, 280051, 280052, 280066, 280107, 280108, 280111, 280114, 280118, 280126, 280131, 280134, 280135, 280140

LHC17o

280282, 280283, 280284, 280285, 280286, 280290, 280310, 280312, 280348, 280349, 280350, 280351, 280352, 280374, 280375, 280403, 280405, 280406, 280412, 280413, 280415, 280419, 280443, 280445, 280446, 280447, 280448, 280490, 280499, 280518, 280519, 280546, 280547, 280550, 280551, 280574, 280575, 280576, 280581, 280583, 280613, 280634, 280636, 280637, 280639, 280645, 280647, 280648, 280650, 280671, 280673, 280676, 280679, 280681, 280705, 280706, 280729, 280753, 280754, 280755, 280756, 280757, 280761, 280763, 280764, 280765, 280766, 280767, 280768, 280786, 280787, 280792, 280793, 280842, 280844, 280845, 280847, 280848, 280849, 280854, 280856, 280880, 280881, 280890, 280897, 280936, 280940, 280943, 280947, 280990, 280994, 280996, 280997, 280998, 280999, 281032, 281033, 281035, 281036, 281079, 281080, 281081, 281179, 281180, 281181, 281189, 281190, 281191, 281212, 281213, 281240, 281241, 281242, 281243, 281244, 281271, 281273, 281275, 281277, 281301, 281321, 281350, 281415, 281441, 281443, 281444, 281446, 281449, 281450, 281475, 281477, 281509, 281511, 281557, 281562, 281563, 281568, 281569, 281574, 281580, 281581, 281583, 281592, 281633, 281705, 281706, 281707, 281709, 281713, 281741, 281750, 281751, 281753, 281754, 281755, 281892, 281893, 281894, 281895, 281915, 281916, 281918, 281920, 281928, 281931, 281932, 281939, 281940, 281953, 281956, 281961

LHC17r

282528, 282544, 282545, 282546, 282573, 282575, 282579, 282580, 282606, 282607, 282608, 282609, 282618, 282620, 282622, 282629, 282651, 282653, 282666, 282667, 282668, 282670, 282671, 282673, 282676, 282677, 282700, 282702, 282703, 282704

LHC18d

285978, 285979, 285980, 286014, 286025, 286027, 286028, 286030, 286064, 286124, 286127, 286129, 286130, 286159, 286198, 286199, 286201, 286202, 286203, 286229, 286230, 286231, 286254, 286255, 286257, 286258, 286261, 286263, 286282, 286284, 286287, 286288, 286289, 286308, 286309, 286310, 286312, 286314, 286336, 286337, 286340, 286341, 286345, 286348, 286349, 286350

LHC18e

286380, 286426, 286427, 286428, 286454, 286455, 286501, 286502, 286508, 286509, 286566, 286567, 286568, 286569, 286591, 286592, 286594, 286653, 286661, 286695, 286731, 286799, 286801, 286805, 286809, 286810, 286846, 286848, 286850, 286852, 286874, 286876, 286877, 286907, 286908, 286910, 286911, 286930, 286931, 286932, 286933, 286936, 286937

LHC18f

287000, 287021, 287063, 287064, 287066, 287071, 287072, 287077, 287137, 287155, 287201, 287202, 287203, 287204, 287208, 287209, 287248, 287249, 287250, 287251, 287254, 287283, 287324, 287325, 287343, 287344, 287346, 287347, 287349, 287353, 287355, 287356, 287360, 287380, 287381, 287385, 287387, 287388, 287389, 287413, 287451, 287480, 287481, 287484, 287486, 287513, 287516, 287517, 287518, 287520, 287521, 287524, 287573, 287575, 287576, 287578, 287654, 287656, 287657, 287658, 287783, 287784, 287876, 287877, 287883, 287884, 287885, 287911, 287912, 287913, 287915, 287923, 287941, 287975, 287977

LHC18g

288687, 288689, 288690, 288743, 288748, 288750

LHC18h

288806

LHC18k

289165, 289166, 289167, 289169, 289172, 289176, 289177, 289198, 289199, 289200, 289201

LHC18l

289240, 289241, 289242, 289243, 289247, 289249, 289253, 289254, 289275, 289276, 289277, 289278, 289280, 289300, 289303, 289306, 289308, 289309, 289353, 289354, 289355, 289356, 289363, 289365, 289366, 289367, 289368, 289369, 289370, 289373, 289374, 289426, 289444, 289462, 289463, 289465, 289466, 289468, 289493, 289494, 289547, 289574, 289576, 289577, 289582, 289625, 289632, 289657, 289658, 289659, 289660, 289664, 289666, 289721, 289723, 289724, 289729, 289731, 289732, 289757, 289775, 289808, 289811, 289814, 289815, 289816, 289817, 289818, 289830, 289849, 289852, 289854, 289855, 289856, 289857, 289880, 289884, 289928, 289931, 289935, 289940, 289941, 289943, 289966, 289971

LHC18m

290293, 290294, 290297, 290298, 290300, 290323, 290324, 290327, 290350, 290374, 290375, 290401, 290404, 290411, 290412, 290423, 290425, 290427, 290428, 290456, 290458, 290459, 290467, 290469, 290499, 290501, 290538, 290539, 290540, 290544, 290549, 290550, 290553, 290590, 290612, 290613, 290614, 290615, 290627, 290632, 290645, 290658, 290660, 290665, 290687, 290692, 290696, 290699, 290721, 290742, 290764, 290766, 290769, 290774, 290776, 290787, 290790, 290841, 290846, 290848, 290853, 290860, 290862, 290886, 290887, 290888, 290892, 290894, 290895, 290932, 290935, 290941, 290943, 290944, 290948, 290974, 290975, 290976, 290979, 290980, 291002, 291003, 291004, 291005, 291006, 291035, 291037, 291041, 291065, 291066, 291093, 291100, 291101, 291110, 291111, 291116, 291143, 291209, 291240, 291257, 291263, 291265, 291266, 291282, 291283, 291284, 291285, 291286, 291360, 291361, 291362, 291363, 291373, 291375, 291377, 291397, 291399, 291400, 291402, 291416, 291417, 291419, 291420, 291424, 291446, 291447, 291451, 291453, 291456, 291457, 291481, 291482, 291484, 291485, 291590, 291614, 291615, 291618, 291622, 291624, 291626, 291657, 291661, 291665, 291690, 291692, 291694, 291697, 291698, 291702, 291706, 291729, 291755, 291756, 291760, 291762, 291766, 291768, 291769, 291795, 291796, 291803, 291942, 291943, 291944, 291945, 291946, 291948, 291953, 291976, 291977, 291982, 292012, 292040, 292060, 292061, 292062, 292067, 292075, 292077, 292080, 292081, 292106, 292107, 292108, 292109, 292114, 292115, 292140, 292160, 292161, 292162, 292163, 292164, 292166, 292167, 292168, 292192, 292240, 292241, 292242, 292265, 292269, 292270, 292273, 292274, 292298, 292397, 292398, 292405, 292406, 292428, 292429, 292430, 292432, 292434, 292456, 292457, 292460, 292461, 292495, 292496, 292497, 292500, 292521, 292523, 292524, 292526, 292553, 292554, 292557, 292559, 292560, 292563, 292584, 292586, 292693, 292695, 292696, 292698, 292701, 292704, 292737, 292739, 292744, 292747, 292748, 292752, 292754, 292758, 292803, 292804, 292809, 292810, 292811, 292831, 292832, 292834, 292836, 292839

LHC18o

293413, 293474, 293475, 293494, 293496, 293497, 293570, 293573, 293578, 293583, 293587, 293588, 293686, 293689, 293691, 293692, 293695, 293740, 293741, 293770, 293773, 293774, 293799, 293802, 293805, 293807, 293809, 293829, 293830, 293831, 293856, 293886, 293891, 293893, 293896, 293898

LHC18p

294009, 294010, 294011, 294012, 294013, 294131, 294152, 294154, 294155, 294156, 294199, 294200, 294201, 294205, 294208, 294210, 294212, 294241, 294242, 294305, 294307, 294308, 294310, 294524, 294525, 294526, 294527, 294529, 294530, 294531, 294553, 294556, 294558, 294563, 294586, 294587, 294588, 294590, 294591, 294593, 294632, 294633, 294634, 294636, 294653, 294703, 294710, 294715, 294716, 294718, 294721, 294722, 294741, 294742, 294743, 294744, 294745, 294746, 294747, 294749, 294769, 294772, 294774, 294775, 294805, 294809, 294813, 294815, 294816, 294817, 294818, 294852, 294875, 294877, 294880, 294883, 294884, 294916, 294925

Appendix C

Additional plots

C.1 Particle Identification

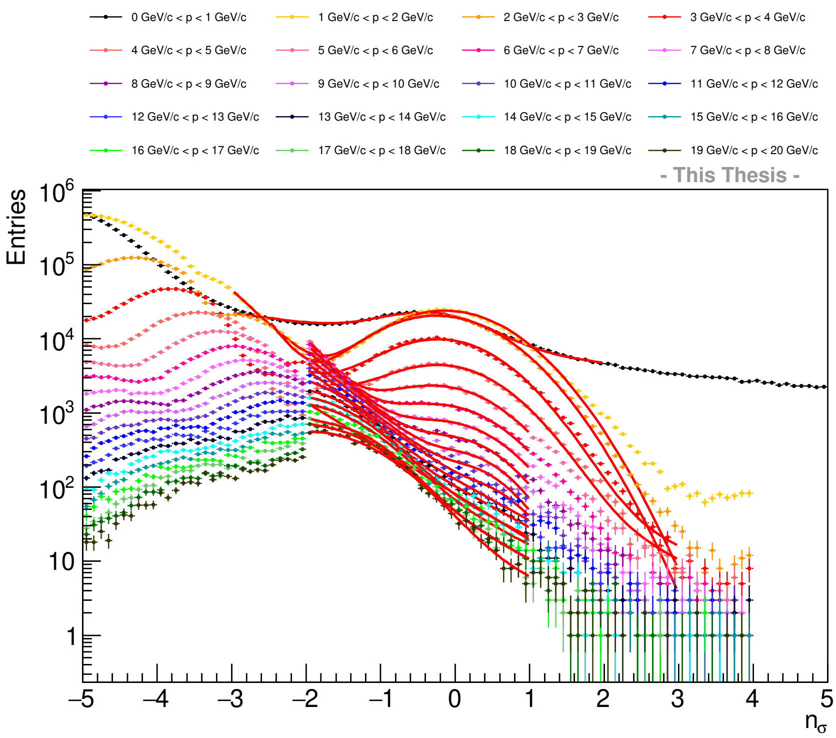

Figure C.1: Projections on TPC n_σ for p-intervals with functional fits shown as red lines as an example for the data taking period LHC18m.

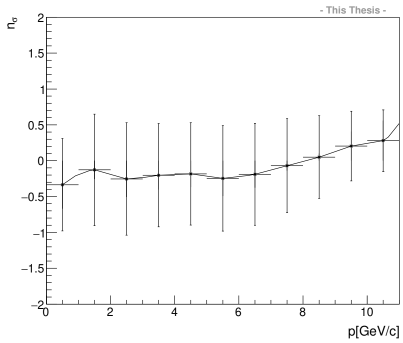

(a) Mean values of n_σ and width from Gaussian fit as error for p-intervals whose width is represented by bars as an example for the data taking period LHC18m.

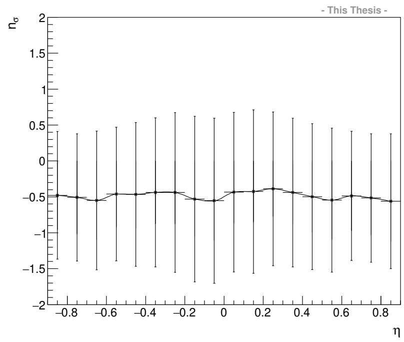

(b) Mean values of n_σ and width from Gaussian fit as error for η-intervals whose width is represented by bars as an example for the data taking period LHC18m.

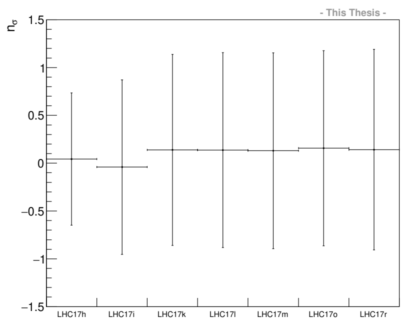

(a) Comparison of the mean value of n_σ for $p_T < 4$ GeV$/c$ for the data taking periods in 2017.

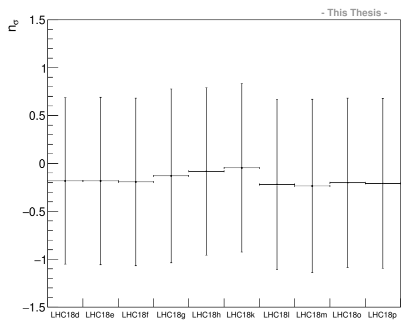

(b) Comparison of the mean value of n_σ for $p_T < 4$ GeV$/c$ for the data taking periods in 2018.

C.1.1 Post-Calibration TPC n_σ - Protons and Pions

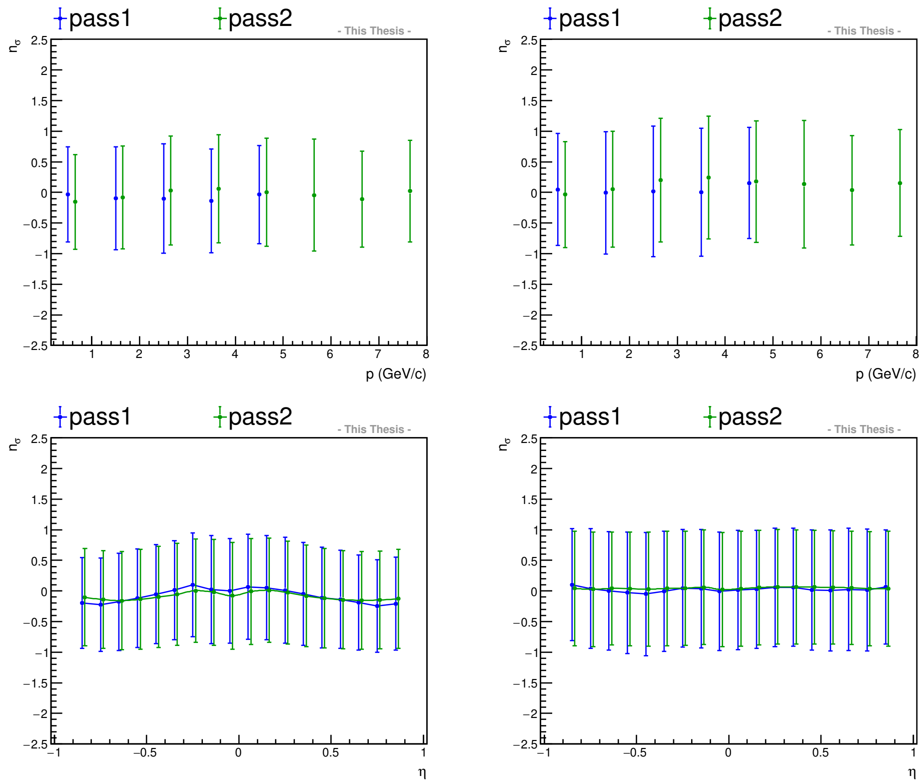

Figure C.4: Mean and width of the Gaussian fit for TPC n_σ vs momentum (top) and pseudorapidity (bottom) for **protons** from the **V0** sample in the LHC18 pass1 and pass2 reconstruction before (left) and after (right) the correction.

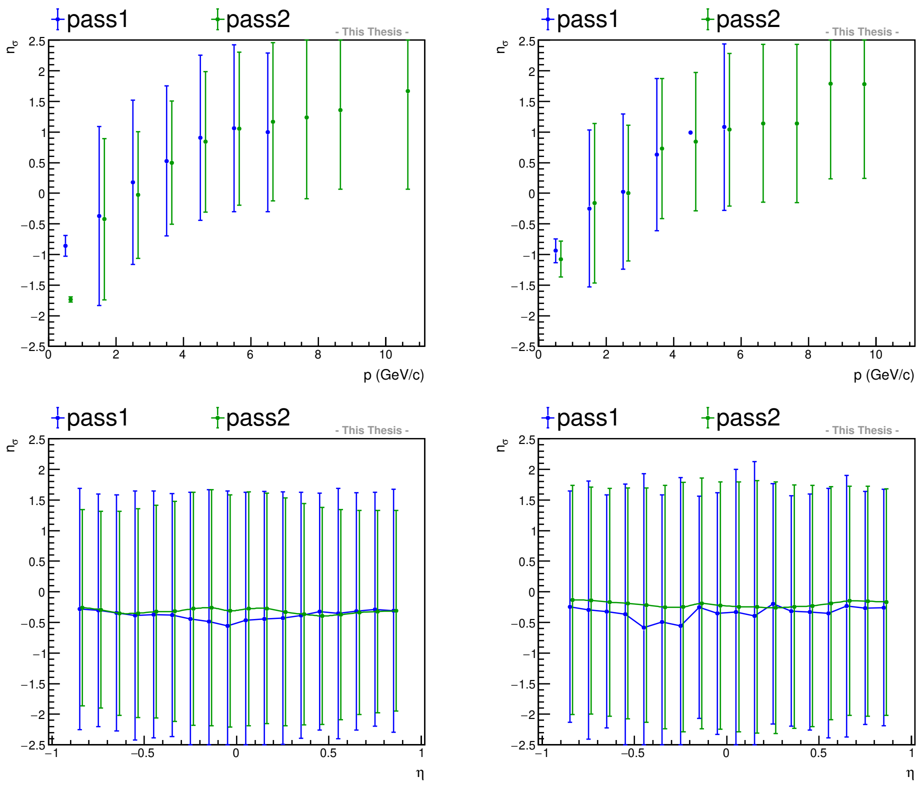

Figure C.5: Mean and width of the Gaussian fit for TPC n_σ vs momentum (top) and pseudorapidity (bottom) for **protons** triggered by the **TRD** in the LHC18 pass1 and pass2 reconstruction before (left) and after (right) the correction.

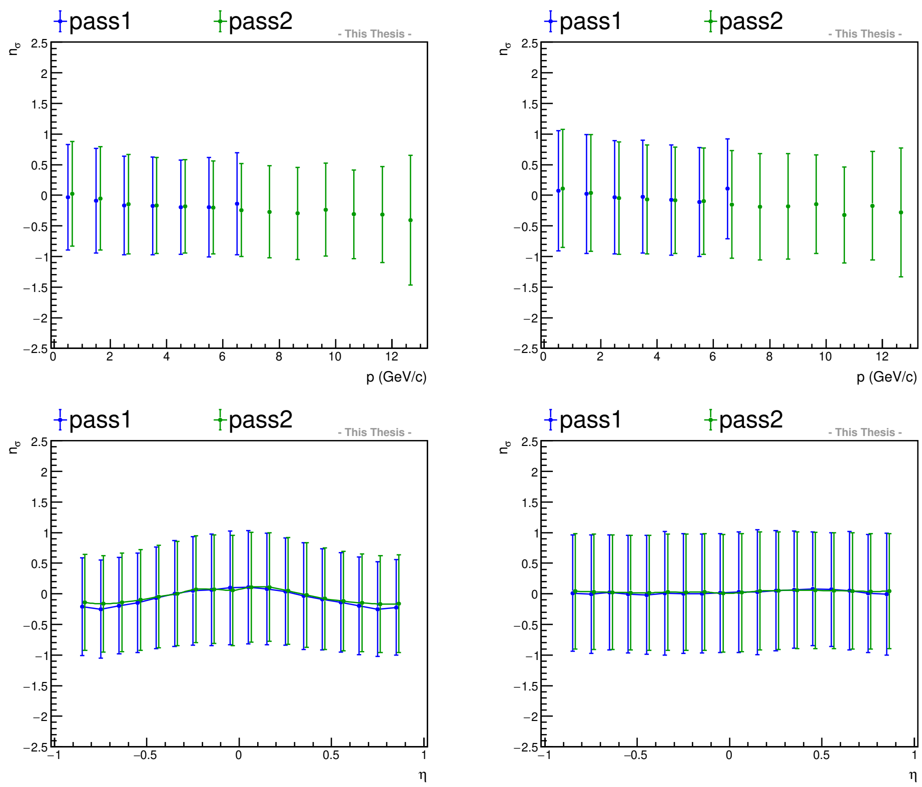

Figure C.6: Mean and width of the Gaussian fit for TPC n_σ vs momentum (top) and pseudorapidity (bottom) for **pions** from the **V0** sample in the LHC18 pass1 and pass2 reconstruction before (left) and after (right) the correction.

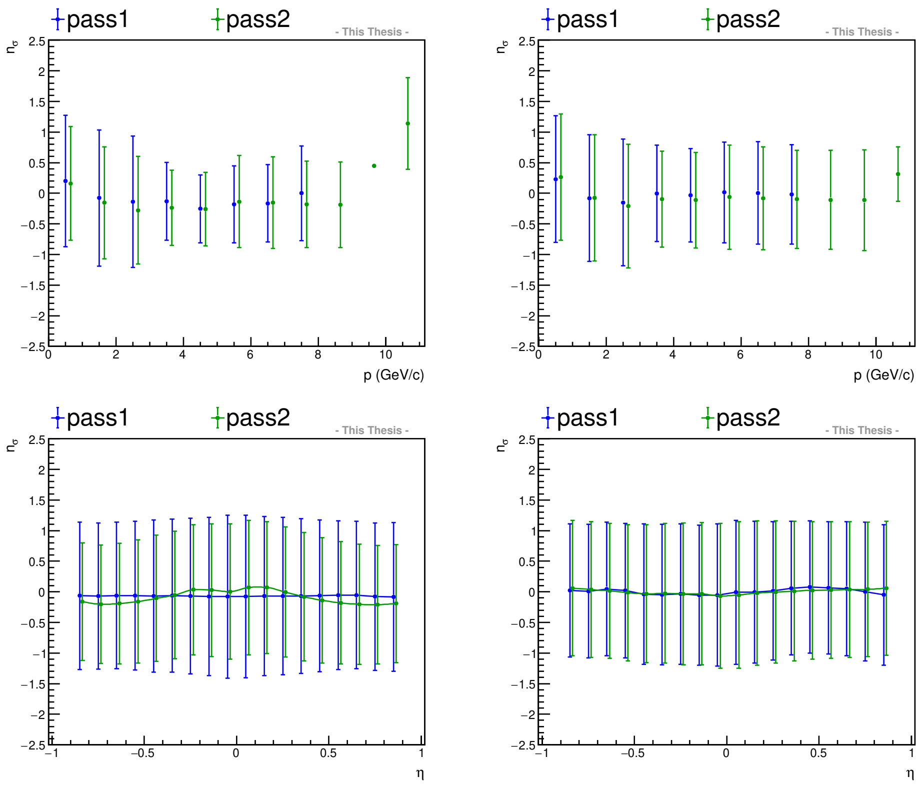

Figure C.7: Mean and width of the Gaussian fit for TPC n_σ vs momentum (top) and pseudorapidity (bottom) for **pions** triggered by the **TRD** in the LHC18 pass1 and pass2 reconstruction before (left) and after (right) the correction.

C.2 Event Quality Assurance

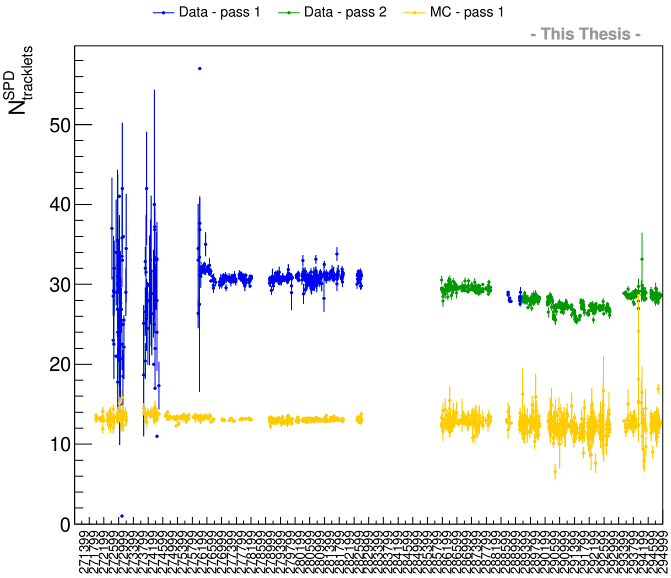

Figure C.8: $N^{\mathrm{SPD}}_{\mathrm{tracklets}}$ vs run number. The labels along the x-axis show the run number for every 400th run.

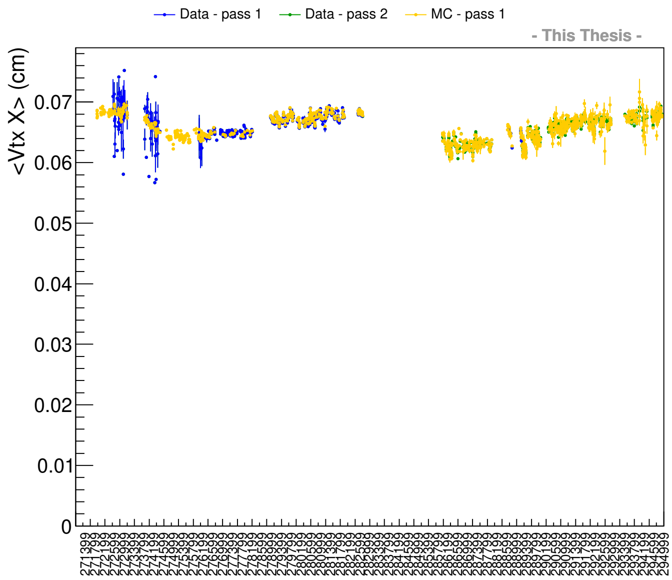

Figure C.9: Average position of the x-vertex for accepted events vs run number. The labels along the x-axis show the run number for every 400th run.

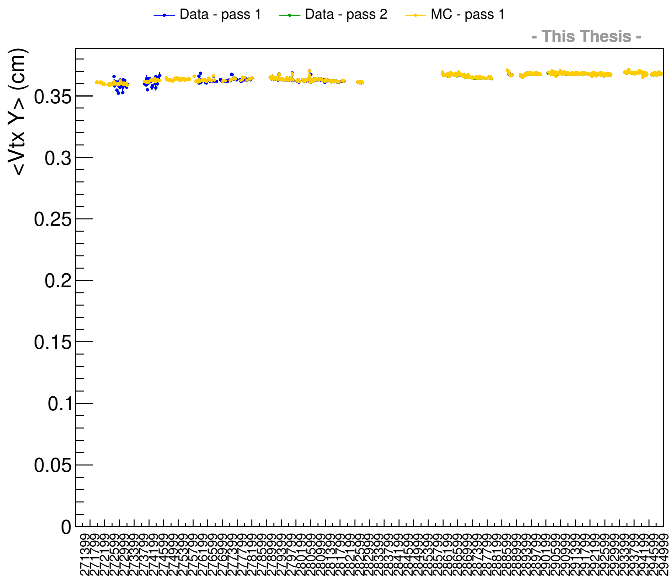

Figure C.10: Average position of the y-vertex for accepted events vs run number. The labels along the x-axis show the run number for every 400th run.

C.3 Electron Track Quality Assurance

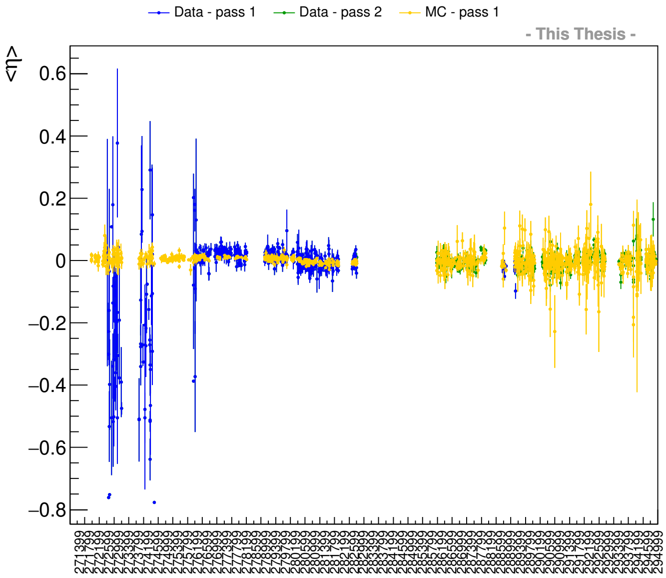

Figure C.11: η vs run number. The labels along the x-axis show the run number for every 400th run.

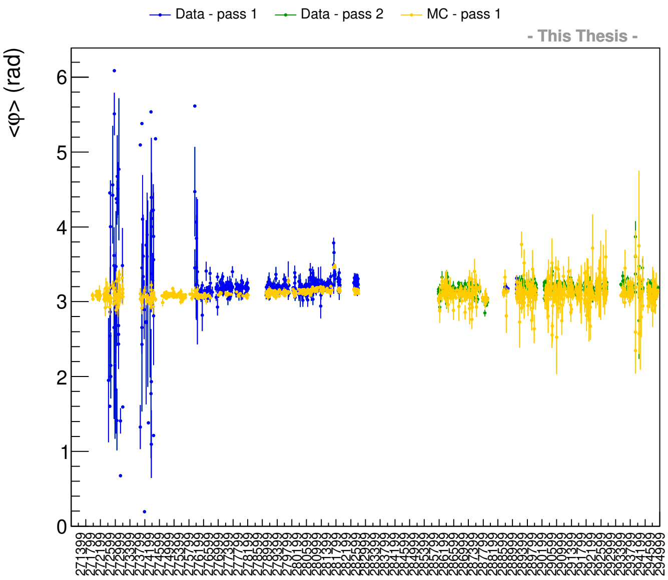

Figure C.12: φ vs run number. The labels along the x-axis show the run number for every 400th run.

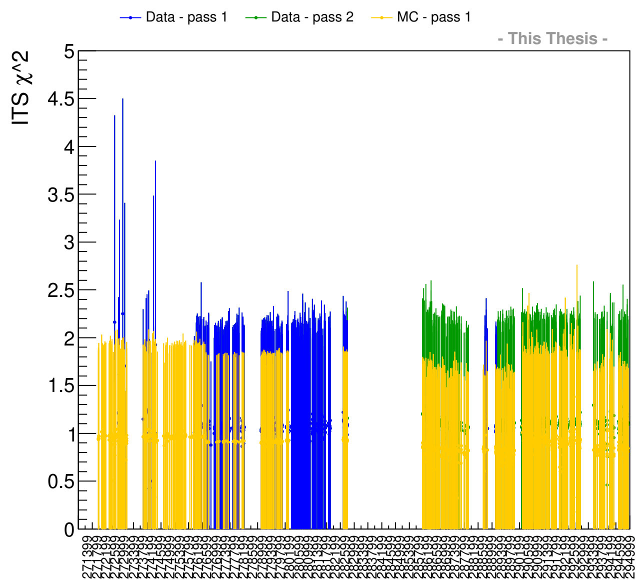

Figure C.13: Average χ^2_{ITS} vs run number. The labels along the x-axis show the run number for every 400th run.

Acknowledgements

First and foremost, I would like to express my deepest gratitude to my supervisor Priv. Doz. Dr. Yvonne Pachmayer for giving me the opportunity to join the ALICE group at PI. I am grateful for her optimistic nature and the patience that she had with me during the online mentoring.

Moreover, I would like to thank Prof. Dr. Johanna Stachel for welcoming me in the group and for kindly accepting to be the second referee for my thesis.

In addition, I would like to thank Minjung Kim for proofreading my thesis and for all the helpful comments and explanations.

Furthermore, I want to thank Ole Schmidt for fixing the issues I had with the Condor Farm.

Additionally, I want to thank the whole ALICE group at PI for welcoming me as a new member and for all the friendly conversations during the Coffee Roulette, on the Discord Server as well as offline.

I also want to express my gratitude to Markus, Mathias, Rafaela and Sara for improving this thesis with their engaged proofreading and to Wiebke for being a reliable partner throughout the whole time of studies.

Further, I want to thank my friends for their encouragement and for lifting me up with countless game nights, walks or conversations on the phone.

Finally, I want to thank my family for their continuous love and support throughout my studies and beyond.

Erklärung

Ich versichere, dass ich diese Arbeit selbstständig verfasst und keine anderen als die angegebenen Quellen und Hilfsmittel benutzt habe.

Dossenheim, den 18.07.2021,

S. Rohletter

Sophie Rohletter

Bibliography

[1] Private communication Y. Pachmayer.

[2] SM Schematics. https://commons.wikimedia.org/wiki/File:Standard_Model_of_Elementary_Particles.svg#file. (last accessed: 8.7.2021).

[3] ALICE collaboration. The ALICE Transition Radiation Detector: construction, operation, and performance. *Nuclear Instruments and Methods in Physics Research Section A: Accelerators, Spectrometers, Detectors and Associated Equipment*, 881:88–127, Feb 2018.

[4] J. J. Aubert et al. Experimental Observation of a Heavy Particle *J. Phys. Rev. Lett.*, 33:1404–1406, 1974.

[5] J. E. Augustin et al. Discovery of a Narrow Resonance in e^+e^- Annihilation. *Phys. Rev. Lett.*, 33:1406–1408, 1974.

[6] ALICE collaboration. ALICE Time Projection Chamber. https://alice-tpc.web.cern.ch/content/alice-time-projection-chamber. (last accessed: 13.7.2021).

[7] ALICE collaboration. The ALICE experiment at the CERN LHC. *JINST*, 3:S08002, 2008.

[8] ALICE collaboration. First results of the ALICE detector performance at 13 TeV. Aug 2015.

[9] ALICE collaboration. Centrality and transverse momentum dependence of inclusive j/ψ production at midrapidity in pb–pb collisions at snn=5.02 tev. *Physics Letters B*, 805:135434, Jun 2020.

[10] David Baumeier. V0 Decays: Documentation of the C++ Program AliESDv0KineCuts.cxx. *Bachelor Thesis, Universität Münster*, 2011.

[11] A. Andronic et al. Decoding the phase structure of QCD via particle production at high energy. *Nature*, 561(7723):321–330, 2018.

[12] J. Alme et al. The ALICE TPC, a large 3-dimensional tracking device with fast readout for ultra-high multiplicity events. *Nuclear Instruments and Methods in Physics Research Section A: Accelerators, Spectrometers, Detectors and Associated Equipment*, 622(1):316–367, Oct 2010.

[13] V. Manzari et al. The silicon pixel detector (SPD) for the ALICE experiment. *Journal of Physics G: Nuclear and Particle Physics*, 30:S1091, 07 2004.

[14] S. L. Glashow, J. Iliopoulos, and L. Maiani. Weak interactions with lepton-hadron symmetry. *Phys. Rev. D*, 2:1285–1292, Oct 1970.

[15] I. Lofnes, L. Altenkämper, I. Arsene. Analysis Note: Inclusive J/ψ - cross section via the di-electron channel in ALICE in MB pp collisions at $\sqrt{s} = 13$ TeV. *ALICE Internal Analysis Note*, 2020.

[16] Hermann Kolanoski and Norbert Wermes. *Teilchendetektoren: Grundlagen und Anwendungen*. Springer, 2016.

[17] T. Matsui and H. Satz. J/ψ Suppression by Quark-Gluon Plasma Formation. *Phys. Lett. B*, 178:416–422, 1986.

[18] Ole Schmidt. Simulation and commissioning of the rejection of late conversions in the TRD triggers of ALICE. *Master Thesis, Universiät Heidelberg*, 2016.

[19] Torbjörn Sjöstrand. The Pythia event generator: Past, present and future. *Computer Physics Communications*, 246:106910, Jan 2020.

[20] Mark Thomson. *Modern Particle Physics*. Cambridge University Press, 2013.

[21] Z. Was, P. Golonka, and G. Nanava. PHOTOS Monte Carlo for precision simulation of QED in decays - History and properties of the project, 2007.

[22] Y. Pachmayer, M. Kim, M.K. Köhler, J. Stachel. Measurement of J/ψ in TRD-triggered p–Pb collisions at $\sqrt{sNN} = 8.16$ TeV with ALICE at the LHC. *ALICE Internal Analysis Note*, 2021.

[23] P.A. Zyla et al. Review of Particle Physics. *PTEP*, 2020(8):083C01, 2020.